Master's Thesis

Layer-by-Layer Assembly of Molecular Metal Oxide Catalysts for Photoelectrochemical Water Splitting

Dasom Jeon

Department of Energy Engineering

(Energy Engineering)

Graduate School of UNIST

2017

Layer-by-Layer Assembly of Molecular Metal Oxide Catalysts for Photoelectrochemical Water Splitting

Dasom Jeon

Department of Energy Engineering

(Energy Engineering)

Graduate School of UNIST

Layer-by-Layer Assembly of Molecular Metal Oxide Catalysts for Photoelectrochemical Water Splitting

A thesis
submitted to the Graduate School of UNIST
in partial fulfillment of the
requirements for the degree of
Master of Science

Dasom Jeon

1. 11. 2017
Approved by

Advisor
Jungki Ryu

Layer-by-Layer Assembly of Molecular Metal Oxide Catalysts for Photoelectrochemical Water Splitting

Dasom Jeon

This certifies that the thesis of Dasom Jeon is approved.

1. 11. 2017

Signature

Advisor: Jungki Ryu

Signature

Byeong-Su Kim

Signature

Hyun-Kon Song

Abstract

Artificial photosynthesis is considered one of the most promising solutions to modern energy and environmental crises. Considering that it is enabled by multiple components through a series of photoelectrochemical processes, the key to successful development of a photosynthetic device depends not only on the development of novel individual components but also on the rational design of an integrated photosynthetic device assembled from them. However, most studies have been dedicated to the development of individual components due to the lack of a general and simple method for the construction of the integrated device. In the present study, we report a versatile and simple method to prepare an efficient and stable photoelectrochemical device via controlled assembly and integration of functional components using the layer-by-layer (LbL) assembly technique. As a proof of concept, we could successfully build a photoanode for photocatalytic water oxidation by modifying the surface of various photoelectrode materials (e.g., Fe_2O_3, $BiVO_4$, and TiO_2) with diverse cationic polyelectrolytes and anionic polyoxometalate (molecular metal oxide) water oxidation catalysts. It was found that the performance of photoanodes was significantly improved after the deposition in terms of stability as well as photocatalytic properties, regardless of types of photoelectrodes and polyelectrolytes employed. Considering the simplicity and universal nature of LbL assembly techniques, we believe that our approach can provide a general and simple method for the design and realization of a novel photosynthetic device.

Contents

Ⅰ. Introduction ---------- 15

1.1 Research Background ---------- 15

1.2 Artificial Photosynthesis ---------- 15

1.3 Research Motivation ---------- 17

1.4 Layer-by-layer (LbL) Self-Assembly ---------- 17

1.5 Polyoxometalates ---------- 18

1.6 Research Objective ---------- 19

Ⅱ. Experimental ---------- 20

2.1 Materials ---------- 20

2.2 Fabrication of Various Photoanodes ---------- 20

2.3 Synthesis of Polyoxometalate-based Water Oxidation Catalysts ---------- 20

2.4 Deposition of (Polyelectrolyte-POM)$_n$ Layers on Various Substrates
using the LbL Assembly Technique ---------- 21

2.5 Characterization ---------- 21

2.6 Photoelectrochemical Characterization ---------- 21

Ⅲ. Results and Discussion ---------- 22

3.1 Experimental design ---------- 22

3.2 Characterization ---------- 24

3.3 Effect of Type of Polyelectrolyte on the Performance of LbL-Modified Hematite Photoanodes ---------- 29

3.4 Effect of the Number of the LbL Bilayers ---------- 31

3.5 LbL-Modification of Various Photoanode Materials ---------- 35

IV. Conclusion ---------- 39

V. References ---------- 40

List of Figures

Figure 1. Natural photosynthesis process for oxidation of water and reduction of cofactors with electrons produced from water splitting by Mn_4CaO_5 catalysts under visible light illumination.

Figure 2. Schematic images showing the principles of (a) natural and (b, c) artificial photosynthesis.

Figure 3. Band edge position of various photoanodes for visible-light driven water splitting.

Figure 4. Layer-by-layer self-assembly (LbL) method for fabrication of more efficient photoanodes compared to bare substrates such as Fe_2O_3, $BiVO_4$, gold, TiO_2 etc.

Figure 5. The structures of common metal oxides (VO_2 and WO_3) and of polyoxometalates such $V_{10}O_{28}^{6-}$ without core transition metal components and tetra cobalt polyoxometalates, $Co_4(H_2O)_2(a\text{-}PW_9O_{34})_2^{10-}$, tested in this study.

Figure 6. Experimental scheme for the layer-by-layer assembly of molecular metal oxide catalysts for photoelectrochemical water splitting. (a) Experimental procedure. (b) Molecular structure of the cationic polyelectrolytes and anionic polyoxometalate water-oxidation catalyst used in the present study. (c) Experimental setup for a photoelectrochemical water splitting to (d) measure and compare the photoelectrochemical performance of samples prepared according to (a).

Figure 7. Catalytic activity of polyoxometalates (POMs). We used three different kinds of POMs, such as $[Co_4(H_2O)_2(a\text{-}PW_9O_{34})_2]^{10-}$ (POM), $[Co_4(H_2O)_2(VW_9O_{34})_2]^{10-}$ (POM(V)), and $(\alpha\text{-}PW_9O_{34})^{9-}$ (POM w/o Co). The catalytic activity of POMs in 80 mM phosphate buffer (pH 8.0) was measured by cyclic voltammetry.

Figure 8. X-ray diffraction patterns showing the formation of various photoanodes on the FTO substrate such as (a) α-Fe_2O_3 (hematite), (b) $BiVO_4$, and (c) anatase TiO_2.

Figure 9. Formation and growth of (b-PEI/POM) layers on hematite using the layer-by-layer assembly method. Morphology of hematite photoanodes (a) without and with (b) five, (c) ten, and (d) twenty layers of (b-PEI/POM) was imaged by scanning electron microscopy. Inset shows the corresponding photograph of the hematite electrode on the FTO substrate. (e) Elemental analysis by X-ray

photoemission spectroscopy (XPS) clearly shows the increase of carbon (C), nitrogen (N), cobalt (Co), phosphorus (P) and tungsten (W) content after the deposition of $(b\text{-PEI/POM})_{10}$ layers on the hematite. (f) The formation and growth of (b-PEI/POM) layers was also studied in situ by quartz crystal microbalance (QCM). Black and red triangles indicate the introduction of polyelectrolyte and POM catalyst solutions, respectively.

Figure 10. In situ analysis of the deposition of polyelectrolytes and POM catalysts by quartz crystal microbalance (QCM). The resonance frequency of a quartz crystal disk coated with gold electrodes was monitored in situ upon sequential treatment with solutions containing cationic polyelectrolytes (such as (a) PDDA, (b) PAH, and (c) l-PEI) and anionic POM catalysts. Black and red triangles indicate the introduction of polyelectrolyte and POM catalyst solutions, respectively.

Figure 11. The formation of $(b\text{-PEI/POM})_{10}$ layers on $\alpha\text{-}Fe_2O_3$ photoanodes was also confirmed by comparing energy dispersive X-ray spectra (a) before and (b) after the LbL treatment as well as electron micrographs (Figure 9).

Figure 12. Formation and growth of (b-PEI/POM) layers on electrode surface using the layer-by-layer assembly method was studied ex situ by (a) UV-visible, (b) Fourier-transform infrared (FT-IR), and (c) Raman spectroscopy.

Figure 13. Influence of types of cationic polyelectrolyte on the photoelectrochemical performance of hematite photoanodes. The performance of different samples was compared by measuring (a) linear sweep voltammetry (LSV) and (b) photocurrent density under visible light illumination with an applied bias of 0.6 V vs. Ag/AgCl and (c) summarized in terms of onset potential for water oxidation and photocurrent density. (d) Graph showing the relationship between the number of bilayers (n), the areal density of POM WOCs on the hematite, and the POM-to-polymer molar ratio for different cationic polyelectrolytes.

Figure 14. Influence of types of cationic polyelectrolyte on the photoelectrochemical performance (especially in terms of photocurrent density) of hematite photoanodes as a function of the applied bias. For comparison, ten bilayers of cationic polyelectrolytes and POMs were deposited on the photoanode. The numbers above each column indicate the degree of enhancement of the photocurrent density of each sample compared to that of the bare one.

Figure 15. Effect of the number of (b-PEI/POM) bilayers (n) on the photoelectrochemical performance (especially in terms of photocurrent density) of the hematite photoanodes as a function of the applied bias. The numbers above each point indicate the degree of enhancement of the photocurrent density of each sample compared to that of the bare one.

Figure 16. Effect of the number of (b-PEI/POM) layers on the photocatalytic performance of the hematite photoanode. The performance of different samples was compared by measuring (a) linear sweep voltammetry (LSV) and (b) photocurrent density under visible light illumination with an applied bias of 0.6 V vs. Ag/AgCl and (c) summarized in terms of onset potential for water oxidation and photocurrent density. (d) Mechanistic scheme explaining the degradation of photoanode performance beyond ten layers of (b-PEI/POM). A three-electrode photoelectrochemical cell was prepared to quantify the total charge transfer by (e) chronoamperogram and (f) the actual amount of gas evolved by gas chromatography to calculate the Faradaic efficiency of the hematite electrode with and without (b-PEI/POM) layers.

Figure 17. Effect of b-PEI on the photocatalytic activity of the hematite photoanode. To investigate the potential role of b-PEI, four different samples were prepared as shown in (a), and their photoelectrochemical performance was evaluated by measuring (b) LSV and (c) photocurrent densities in the presence and absence of visible light irradiation.

Figure 18. Stability of hematite photoanodes with and without $(b\text{-PEI/POM})_{10}$ layers. (a) The Pourbaix diagram for $Fe\text{-}H_2O$ was obtained from the Materials Project database (http://www.materialsproject.org). (b) SEM micrographs of hematite with and without $(b\text{-PEI/POM})_{10}$ layers were compared before and after the photoelectrochemical test for 1 h with an applied bias of 0.6 V vs. Ag/AgCl under visible light irradiation to study the effect of $(b\text{-PEI/POM})_{10}$ layers on the stability of hematite photoanodes.

Figure 19. The formation of $(b\text{-PEI/POM})_n$ layers on (a, b) $BiVO_4$ and (c, d) TiO_2 photoanodes was confirmed by comparing energy dispersive X-ray spectra (a, c) before and (b, d) after the LbL treatment, as well as electron micrographs (Figure 15 in the manuscript). Note that the numbers of (b-PEI/POM) bilayers (n) formed on $BiVO_4$ and TiO_2 photoanodes are 10 and 5, respectively.

Figure 20. Improvement of the performance of (a-c) $BiVO_4$ and (d-f) TiO_2 photoanodes using the layer-by-layer (LbL) assembly of cationic polyelectrolyte b-PEI and anionic POM water oxidation catalysts (WOCs). The formation of $(b\text{-PEI/POM})_n$ layers on $BiVO_4$ (n=10) and TiO_2 (n=5) photoanodes was confirmed by (a, b, d, e) electron microscopy, respectively, (a, d) before and (b, e) after the LbL

treatment. (c, f) The effect of the (b-PEI/POM)$_n$ layers on the performance of (c) $BiVO_4$ and (f) TiO_2 photoanodes was studied by measuring the linear sweep voltammetry (LSV) and photocurrent density with and without light irradiation. Note that visible and UV light was illuminated for $BiVO_4$ and TiO_2, respectively.

Figure 21. Photoelectrochemical performance of hematite photoanodes after the deposition of different polyoxometalate catalysts. Although POM(V) had a much higher catalytic activity than POM(P), as shown in Figure S1, POM(V) was found to be less active when integrated on the surface of the hematite photoanode using the LbL assembly method. (a) Molecular structure of POM(P) and POM(V). The photocatalytic performance of each sample was analyzed by measuring (b) linear sweep voltammetry and (c) photocurrent density.

List of Tables

Table 1. Properties of cationic and anionic polyelectrolytes used in the present study.

Table 2. Enhancement of photoelectrochemical performance of $BiVO_4$ and TiO_2 photoanodes by the deposition of (b-PEI/POM) layers.

Nomenclature

WOCs	Water oxidation catalysts
LbL	Layer-by-layer self-assembly
PDDA	Poly(diallyldimethylammonium chloride)
PAH	Poly(allylamine hydrochloride)
b-PEI	Branched poly(ethyleneimine)
l-PEI	Linear poly(ethyleneimine)
POMs	Polyoxometalates
LSV	Linear sweep voltammogram
SEM	Scanning electron microscopy
EDS	Energy-dispersive X-ray spectroscopy
FT-IR	Fourier-transform infrared spectroscopy
QCM	Quartz crystal microbalance
PB	Phosphate buffer
PEs	Polyelectrolytes
XPS	X-ray photoelectron spectroscopy
XRD	X-ray diffraction

I. INTRODUCTION

1.1 Reseach Background

Development of alternative energy resources is getting more and more important in our lives due to a lack of fossil fuel, change of climate, and pollution (Hammarston and Hammes-Schiffer, 2009). Among various alternative energy resources such as wind, biomass, tidal, and solar energy, hydrogen is one of the most promising alternatives to fossil fuels because of its clean and sustainable nature and relatively high energy efficiency (Hammarstom et al., 2011; Ozzie, 2012). There are several methods for the production of hydrogen fuel such as separation of side products from combustion gas of fossil fuels, steam reforming from hydrocarbons, and electrolysis of water (Ilbas et al., 2005; Ming et al., 2002; Holladay et al., 2009). In case of combustion and steam reforming from hydrocarbons process, however, high temperature and pressure are essentially needed to break the bonds in hydrocarbons. These processes lead to the emission of pollutant gases, resulting in serious climate changes. For electrolysis of water, it is a relatively simple method and uses water as an unlimited and clean source (Clifford et al., 2009; Katz et al., 2015). However, it requires electricity produced mostly by non-sustainable methods.

1.2 Artificial Photosynthesis

Artificial photosynthesis mimicking the Mother Nature is one of the most promising methods for the production of hydrogen without any external power supply. In natural photosynthesis, plants utilize electrons produced from solar oxidation of water for the reduction of cofactors, which can provide energy to drive a series of biochemical reactions for the synthesis of glucose molecules from carbon dioxide (Wang et al., 2011). In artificial photosynthesis, useful chemicals or fuels (e.g., hydrogen, methanol, methane, formate, etc.) can be photocatalytically produced using unlimited solar energy and water through a series of photoelectrochemical processes (Figure 1, 2) (Ciamician, 1912).

In principle, any kinds of semiconducting materials with a proper band gap and band edge position can be utilized for oxidation and reduction of water to produce chemicals under visible light illumination. For example, many scientists and engineers have focused on hematite photoanodes due to its abundance, reasonable price and its proper band gap (~2.1 eV) for water oxidation under visible light irradiations (Figure 3) (Jubb et al., 2010; Kim et al., 2014). However, some weaknesses of hematite still remain such as low absorption coefficient, poor hole transfer efficiency and low photoelectrochemical performances (Jubb et al., 2010; Kim et al., 2014; Tamirat et al., 2016; Kim et al., 2013; Shen et al., 2013). To address these issues, many scientists have studied about controlling the thickness of hematite films to enhance the absorption coefficient, fabricating various hematite nanostructures such as nano-cones, -tubes, -sheets, -rods or -wires (Tamirat et al., 2016), and modifying the surface of hematite with

water oxidation catalysts (WOCs) (Kim et al., 2013; Shen et al., 2013).

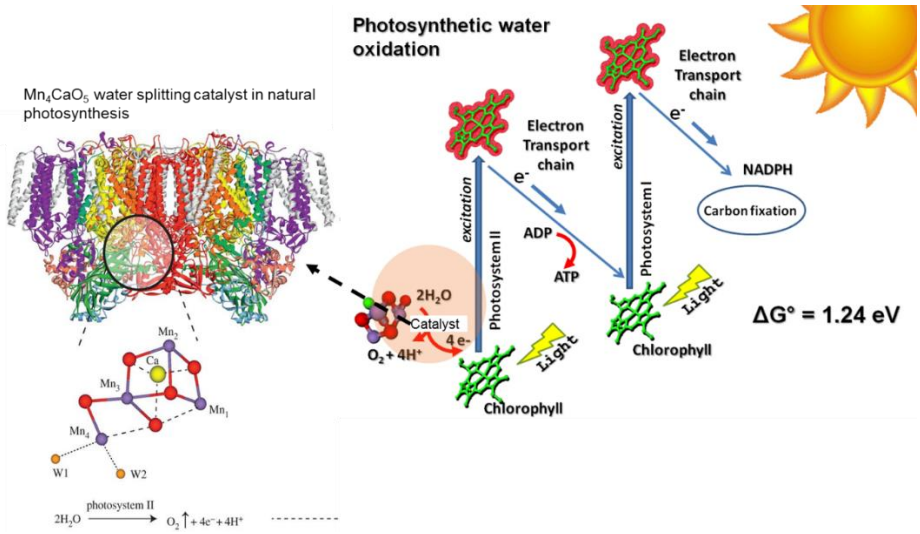

Figure 1. Natural photosynthesis process for oxidation of water and reduction of cofactors with electrons produced from water splitting by Mn_4CaO_5 catalysts under visible light illumination (Cox et al., 2015).

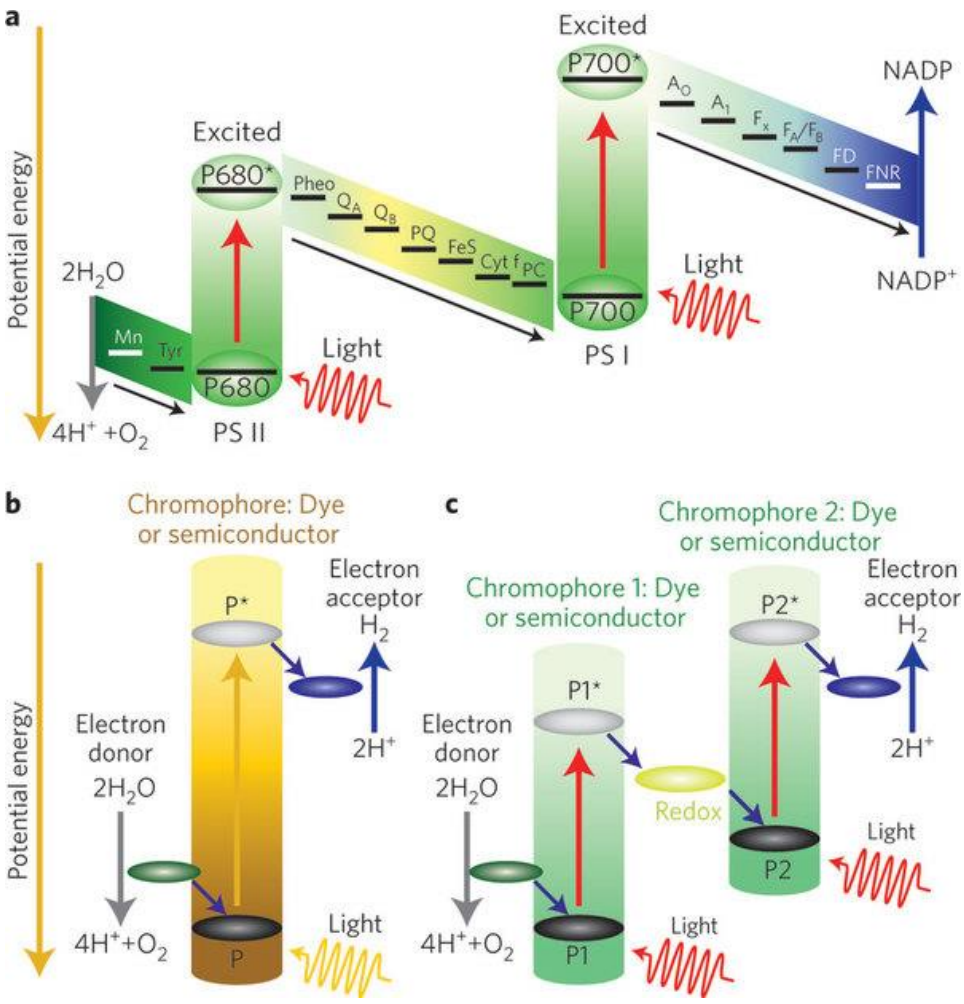

Figure 2. Schematic images showing the principles of (a) natural and (b, c) artificial photosynthesis (Shimada et al., 2012; Tachibana et al., 2012).

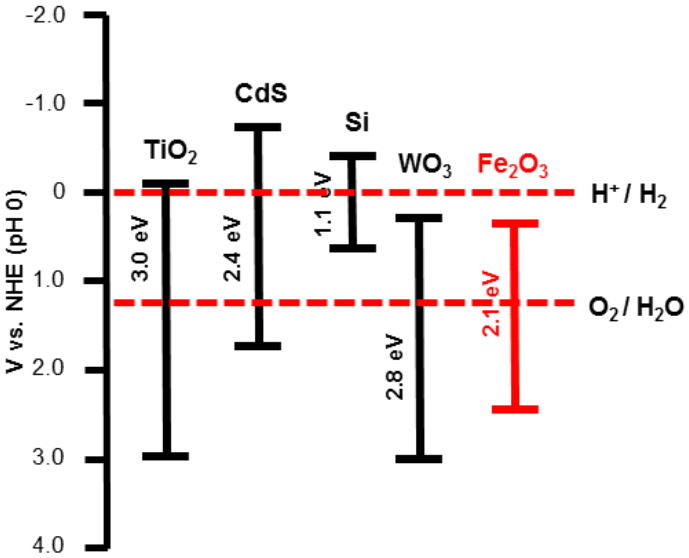

Figure 3. Band edge position of various photoanodes for visible-light driven water splitting.

1.3 Research Motivation

Despite the huge potential of artificial photosynthesis and numerous efforts made to date (Roger et al., 2017), its practical application is still not realized due to low efficiency and stability of photosynthetic devices. Actually, there have been numerous reports on the synthesis and excellent properties of various photosynthetic components. Considering that artificial photosynthesis is enabled by multiple components through a series of photoelectrochemical processes, the key to successful development of a photosynthetic device depends not only on the development of novel individual components but also on the rational design of an integrated photosynthetic device assembled from them. In this regard, the failure to date may be partly due to the absence of a general and simple method to precisely assemble various functional components into a photosynthetic device (White et al., 2015; Kim et al., 2015).

1.4 Layer-by-Layer (LbL) Self-Assembly

In the present study, to improve photoelectrochemical properties of photoelectrodes, we introduced simple and general layer-by-layer self-assembly (LbL) method for the deposition of WOCs on a target substrate . This method allows ready fabrication of films by alternately stacking positively and negatively charged materials with diver sizes and shapes in various combinations on a target substrate through electrostatic interactions (Figure 4) (Xiao et al., 2016). In addition, physical and chemical properties of each component is hardly changed even after the LbL deposition.

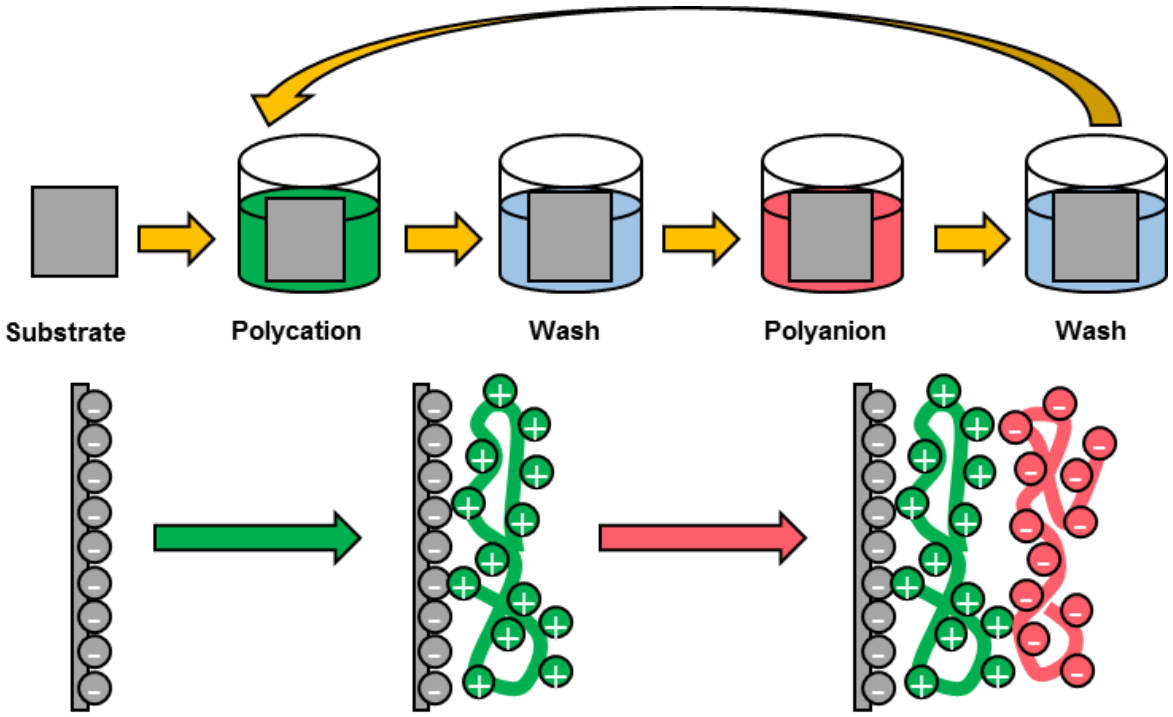

Figure 4. Layer-by-layer self-assembly (LbL) method for fabrication of more efficient photoanodes compared to bare substrates such as Fe_2O_3, $BiVO_4$, gold, TiO_2 etc.

1.5 Polyoxometalate

Polyoxometalates (POMs) are a molecular oxide cluster which can possess polynuclear transition metal complexes. Depending on properties of transition metals, POMs can find versatile applications such as nanomedicine, energy-conversion devices, light-emitting devices, and catalysis. For example, it is reported that anionic POMs can be used in various study fields, such as drug delivery systems by electrostatic interactions with acrylic acid-gelatin components under different pH conditions (Chen et al., 2014; Macon et al., 2016), biosensing by using with noble metals and graphene (Liu et al., 2012) and hybrid supercapacitors with a enhanced stability (Suarez-Guevara et al., 2014). Recently, it is also reported that POMs embedding a tetracobalt-oxo complex have a structure similar to the active site of WOCs in natural photosynthesis (which is composed of tetra manganese core metals and has distorted Cubane-like structure) and cat as a highly stable molecular WOCs. Compared to conventional metal oxide heterogeneous catalysts, POMs have many advantages such as high solubility in water, low absorbance, and high stability against hydrolytic and thermal stress (Figure 5).

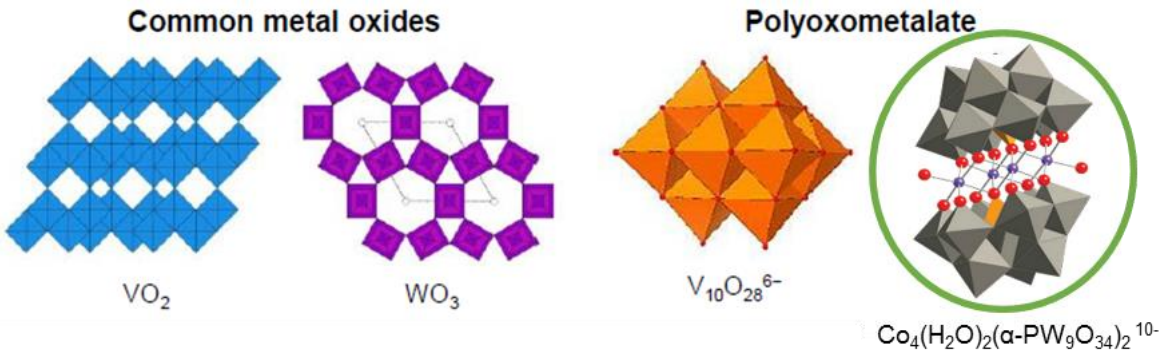

Figure 5. The structures of common metal oxides (VO_2 and WO_3) and of polyoxometalates such $V_{10}O_{28}^{6-}$ without core transition metal components and tetra cobalt polyoxometalates, $Co_4(H_2O)_2(a\text{-}PW_9O_{34})_2^{10-}$, tested in this study.

1.6 Research Objective

We ultimately aimed to fabricate photoanodes with high efficiency and stability using the LbL method. To achieve this goal, positively charged polyelectrolytes and negatively charged WOCs were chosen as LbL components to improve the performance of various photoelectrodes. Various kinds of substrates (e.g., hematite (α-Fe_2O_3), gold, bismuth vanadate ($BiVO_4$), and titania (TiO_2), cationic electrolytes (e.g., poly(diallyldimethylammonium chloride) (PDDA), poly(allyl hydrochloride) (PAH), branched poly(ethyleneimine) (b-PEI) and linear poly(ethyleneimine) (l-PEI)), and anionic POM WOCs were tested. The photoelectrochemical performance of the LbL-modified electrode was evaluated by measuring photocurrent response (e.g., LSV, photocurrent density) and the amount of oxygen and hydrogen gases evolved.

II. EXPERIMENTAL

2.1 Materials

PDDA, PAH, b-PEI, iron chloride, titanium oxide P25, fluorine doped tin oxide glass, iodine doped tin oxide glass, bismuth nitrate, potassium iodide, nitric acid, p-benzoquinone, sodium hydroxide, cobalt nitrate, sodium tungstate, sodium phosphate dibasic and sodium chloride were purchased from Sigma Aldrich (St. Louis, MO, USA). Linear polyethyleneimine and sodium nitrate was produced by Alfa Aesar (Ward Hill, MA, USA). The gold-coated quartz crystal disk was obtained from Stanford Research Systems (Sunnyvale, CA, USA).

2.2 Fabrication of Various Photoanodes

Hematite photoanodes were prepared by a simple hydrothermal method (Jang et al., 2015). Briefly, a clean FTO substrate was prepared, loaded in a 50 mL Teflon-lined stainless steel autoclave containing a 10 mL aqueous solution of 0.15 M $FeCl_3$ and 1.0 M $NaNO_3$, and treated at 100 ^oC for 1 h to grow FeOOH film. Tin-doped hematite film was prepared by annealing the FeOOH film on FTO at 800 ^oC in air for 5 min. The overall process was repeated one more time to obtain high-quality hematite photoanodes. Nanoporous TiO_2 photoanodes were fabricated by using a doctor-blade method (Hoang et al., 2013). Briefly, TiO_2 paste was prepared by ultrasonically mixing 1 g of commercially available TiO_2 nanoparticles with 10 mL of ethanol for 30 min and adding 3 % of titanium isopropoxide to the mixture under vigorous stirring. TiO_2 paste was then casted on ITO by the doctor-blade method and annealed at 150 ^oC for 1 h to obtain nanoporous TiO_2 film. $BiVO_4$ photoanodes were obtained by electrochemical deposition of BiOI film on FTO and its chemical conversion to $BiVO_4$ according to the literature (Jang et al., 2015). A precursor solution for electrodeposition of BiOI was prepared by dissolving $Bi(NO_3)_3$ (0.04 M) in 50 mL of 0.4 M KI solution, adjusting the pH of the solution to 1.7 with HNO_3, and then mixing with 20 mL of 0.23 M p-benzoquinone solution in ethanol. The electrodeposition of BiOI was carried out with a WMPG1000 multichannel potentiostat/galvanostat (WonATech Co. Ltd., Korea) under the following conditions: working electrode, FTO glass; reference electrode, Ag/AgCl; counter electrode, Pt wire; applied potential, -0.1 V vs. Ag/AgCl. The BiOI electrode was converted to $BiVO_4$ by treating it in the presence of 0.2 M vanadyl acetylacetonate at 400 ^oC with a ramping rate of 2 ^oC/min and selectively removing unwanted V_2O_5 with 1 M NaOH solution.

2.3 Synthesis of Polyoxometalate-based Water Oxidation Catalysts

A tetracobalt-substituted POM WOC, $[Co_4(H_2O)_2(PW_9O_{34})_2]^{10-}$ was synthesized according to the literature (Yin et al., 2010). Briefly, the sodium salt of POM was produced by preparing a neutral aqueous solution of 1.08 M $Na_2WO_4 \cdot 2H_2O$, 0.12 M Na_2HPO_4, 0.24 M $Co(NO_3)_2 \cdot 6H_2O$ and refluxing it

at 100 ºC for 2 h. The resultant POM WOCs were purified by recrystallization.

To synthesize $Na_{10}[Co_4(H_2O)_2(VW9O_{34})_2]$ (POM(V)), firstly, 1.2 g of $Co(NO_3)_2{\cdot}6H_2O$ and 6.0 g of $Na_2WO_4{\cdot}2H_2O$ was dissolved in 0.5 M sodium acetate buffer (120 mL, pH 4.8) and vigorously stirred for approximately 5 minutes. 0.27 g of $NaVO_3$ was added to the above solution. The resulting mixture was heated to 80 ºC for 2 h. The hot brown solution was filtered to remove any precipitates and left to crystallize. The crystallized product was extracted and $Na_{10}[Co_4(H_2O)_2(VW9O_{34})_2]{\cdot}35H_2O$ by vacuum filtration and dried under vacuum (Lv et al., 2014).

2.4 Deposition of (Polyelectrolyte-POM)$_n$ Layers on Various Substrates using the LbL Assembly Technique

For the integration of negatively charged POM catalysts using the LbL assembly technique, we used four different cationic polyelectrolytes: b-PEI, l-PEI, PAH, and PDDA. For LbL assembly, cationic polyelectrolytes and anionic POMs were dissolved at 3 mM (in terms of monomer concentration) and 1 mM, respectively, in a 10 mM phosphate buffer with 137 mM of NaCl (pH 5.0). One cycle of LbL assembly consists of sequential treatment of the substrate with polyelectrolyte and POM solutions for 5 min each. The substrate was washed with deionized water for 30 s three times between each cycle and treated repeatedly for the desired number of times (n).

2.5 Characterization

Morphology and elemental composition of samples were characterized by an S-4800 scanning electron microscope (SEM) (Hitachi High-Technologies, Japan) equipped with an elemental energy-dispersive X-ray spectroscope (EDS). The formation of (polyelectrolyte-POM) layers on various electrodes was confirmed with multiple analytical tools such as a V-730 UV-Visible spectrophotometer (JASCO, Japan), a Cary 670/620 Fourier-transform infrared (FT-IR) microscope (Agilent Technologies, Santa Clara, CA, USA), an alpha 300R confocal Raman microscope (WITec, German), and a QCM200 quartz crystal microbalance (QCM) (Stanford Research Systems, Sunnyvale, CA, USA).

2.6 Photoelectrochemical Characterization

The photoelectrochemical performance of photoelectrodes was characterized by LSV in the presence and absence of visible light irradiation with a WMPG1000 multichannel potentiostat/galvanostat under the following conditions: working electrode, photoelectrodes with and without the LbL modification; reference electrode, Ag/AgCl; counter electrode, Pt wire; electrolyte, 80 mM phosphate buffer (PB, pH or 8); visible light source, 300W Xe lamp equipped with a 400 nm cut-on filter. Evolution of oxygen and hydrogen gas during the photoelectrochemical test was identified and quantified with a GC-2010 Plus gas chromatograph (Shimadzu Co., Japan). All measurements were done at least in triplicate for statistical analysis.

III. RESULTS & DISCUSSION

3.1 Experimental Design

To demonstrate the validity of our approach for the development of an artificial photosynthetic device, we designed a series of experiments to construct various photoanodes (i.e., half-cell devices) for visible-light driven water oxidation using the LbL assembly technique (Figure 6). Note that photocatalytic oxidation of water is a critical step to provide electrons for the production of target chemicals via electrocatalytic reduction. In brief, various substrates (e.g., FTO, ITO, Fe_2O_3, TiO_2, $BiVO_4$, Au, and etc.) were sequentially treated with cationic PEs and anionic molecular oxide catalysts for the desired number of times (Figure 6a). Here, we tested four different kinds of cationic PEs (Figure 6b) such as b-PEI, l-PEI, PAH, and PDDA for the integration of molecular WOCs onto a desired substrate. Properties of these polyelectrolytes are summarized in Table 1. A tetracobalt-substituted polyoxometalate $[Co_4(H_2O)_2(PW_9O_{34})_2]^{10-}$ (POM) (Figure 6b) was chosen as a model WOC because it is well-known as an efficient hole scavenger and stable molecular WOC with multiple negative charges (Sartorel et al., 2008; Yin et al., 2010; Orlandi et al., 2010; Toma et al., 2010; Lauinger et al., 2015). The performance of various photoanodes before and after the LbL modification was then evaluated by constructing a photoelectrochemical cell (Figure 6c) and measuring LSV and areal photocurrent density in the presence and absence of light irradiation (Figure 6d). For convenience, A-(PE-POM)$_n$ indicates that an electrode A is modified with the number of bilayers (n) composed of cationic PEs and anionic POM catalysts.

Table 1. Properties of cationic and anionic polyelectrolytes used in the present study.

Polyelectrolytes	Manufacturer	pKa	Molecular weight* (g mol^{-1})
Branched poly(ethyleneimine) (b-PEI)	Sigma-Aldrich	4.5 (primary) 6.7 (secondary) 11.6 (tertiary)	M_n ~10,000 M_w ~ 25,000
Linear poly(ethyleneimine) (l-PEI)	Sigma-Aldrich	9.7	M_n ~10,000
Poly(diallyldimethylammonium chloride) (PDDA)	Sigma-Aldrich	-	M_w ~ 200,000-350,000
Poly(allylamine hydrochloride) (PAH)	Alfa Aesar	8.5	M_w ~ 120,000~200,000
Poly(styrene sulfonate) (PSS)	Sigma-Aldrich	~ 1.0	M_w ~ 70,000

*Molecular weight of polyelectrolytes provided by the manufacturer. M_n and M_w indicate number and weight average molecular weight, respectively.

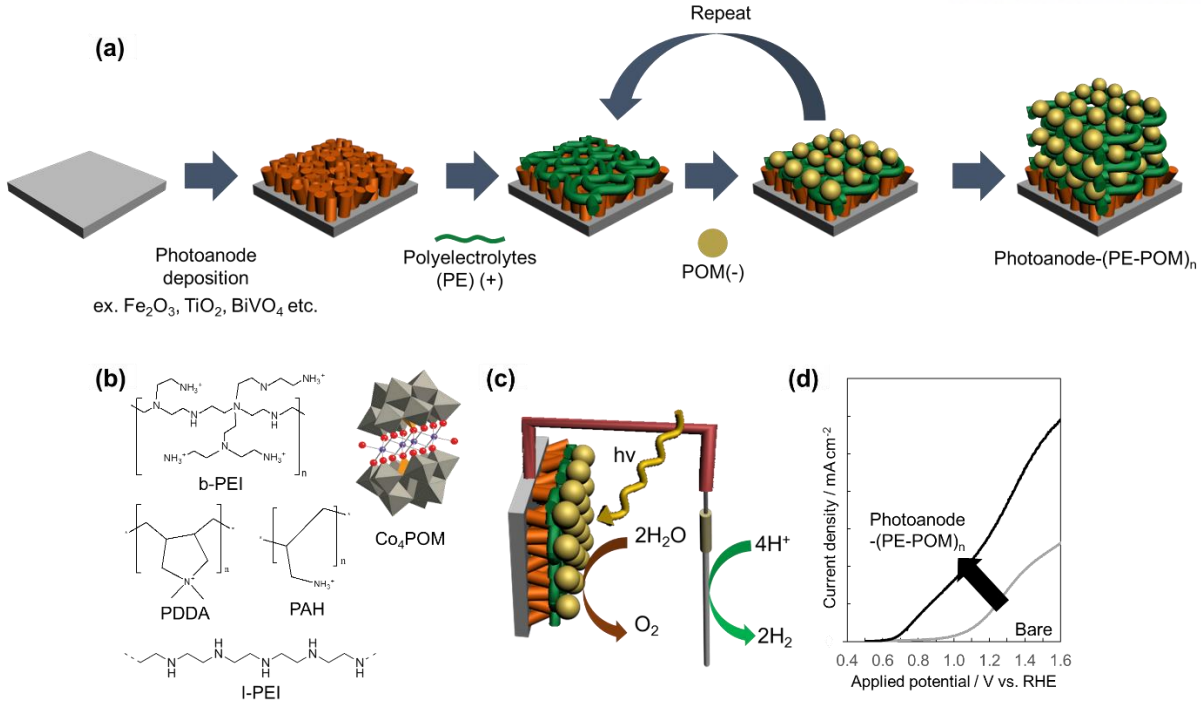

Figure 6. Experimental scheme for the layer-by-layer assembly of molecular metal oxide catalysts for photoelectrochemical water splitting. (a) Experimental procedure. (b) Molecular structure of the cationic polyelectrolytes and anionic polyoxometalate water-oxidation catalyst used in the present study. (c) Experimental setup for a photoelectrochemical water splitting to (d) measure and compare the photoelectrochemical performance of samples prepared according to (a).

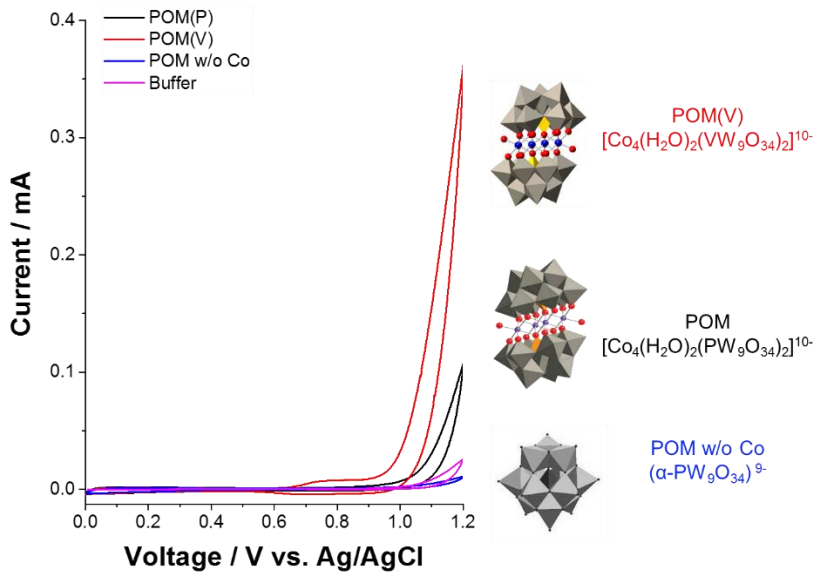

Figure 7. Catalytic activity of polyoxometalates (POMs). We used three different kinds of POMs: $[Co_4(H_2O)_2(a\text{-}PW_9O_{34})_2]^{10-}$ (POM), $[Co_4(H_2O)_2(VW_9O_{34})_2]^{10-}$ (POM(V)), and $(\alpha\text{-}PW_9O_{34})^{9-}$ (POM w/o Co). The catalytic activity of POMs in 80 mM phosphate buffer (pH 8.0) was measured by cyclic voltammetry.

3.2 Characterization

First of all, we studied the effect of type of PEs on the integration of POM WOCs onto a desired substrate using the LbL assembly. Among various substrates, we initially tested α-Fe_2O_3 (hematite) because of its prominent strengths and weaknesses. Hematite is considered as one of the most promising photoanode materials for visible-light driven water splitting due to its narrow bandgap and earth abundance (Sivula et al., 2011; Kim et al., 2014; Tilley et al., 2010; Jang et al., 2015). However, there are many issues to be solved for its practical applications, especially the fast recombination rate of photogenerated electron and hole pairs and needs for a large overpotential for water splitting (Sivula et al., 2011). In this regard, it was believed that hematite can be used as a model photoanode material to test the validity of our approach by modifying it with POM WOCs in various combinations using the LbL assembly and then studying its photoelectrochemical properties. Tin-doped hematite film was readily prepared using the hydrothermal method according to the literature (Jang et al., 2015), and fabrication of hematite films was confirmed by X-ray diffraction (XRD) (Figure 8a). The integration of molecular POM WOCs onto the surface of hematite through LbL method was observed by SEM, elemental analysis with X-ray photoelectron spectroscope (XPS) and EDS. For example, SEM images showed a morphologically clear difference in the hematite photoanode before (Figure 9a) and after (Figure 9b-d) the LbL modification with b-PEI and POM. After ten or more cycles of LbL assembly with b-PEI and POM, a thin layer of aggregates was uniformly coated on the entire electrode surface and visible even with the naked eyes (insets in Figure 9a and 9c). The XPS (Figure 9e) and EDS (Figure 10) spectra indicated the deposition of b-PEI and POM on hematite films due to relative increase of carbon (C) / nitrogen (N) and cobalt (Co) / phosphorus (P) / tungsten (W) content after fabrication of LbL films. The formation of $(PE\text{-}POM)_n$ layers using the LbL assembly was also obviously determined by in situ quartz crystal microbalance (QCM) analysis and ex situ spectroscopies. For in situ QCM analysis (Johannsmann, 2014), a gold-coated quartz crystal disk was used instead of hematite photoanode. We could observe the formation of $(PE\text{-}POM)_n$ layers by monitoring the change of mass upon treatment with a PE and POM solution, regardless of type of cationic PE employed (i.g., b-PEI, l-PEI, PAH, and PDDA) (Figure 9f and Figure 11). The formation of the LbL film on hematite was also investigated ex situ by UV-visible absorbance, Fourier transform infrared (FT-IR), and Raman spectroscopies (Figure 12). UV-visible spectra of hematite photoanode showed a gradual increase of absorbance throughout the entire spectral region with increase of the LbL cycles. It might be due to the enhanced scattering of light by the formation and growth of thin-layer of (b-PEI/POM) aggregates, which was also supported by FT-IR and Raman spectra. The peaks for 490 cm^{-1}, 883, 887 cm^{-1}, 982 cm^{-1}, 1600 cm^{-1} and 3500 cm^{-1} indicates Fe-O, W-O-W, P-O, H-O-H, N-H and O-H bonding, respectively in FT-IR spectra (Jubb et al., 2010; Ryu et al., 2014). 223-611 cm^{-1} Fe-O, 813, 905 cm^{-1} W-O, 966 cm^{-1} P-O, 1320 cm^{-1} Fe-O bonding peaks were shown in Raman spectra (Molchan et al., 2013).

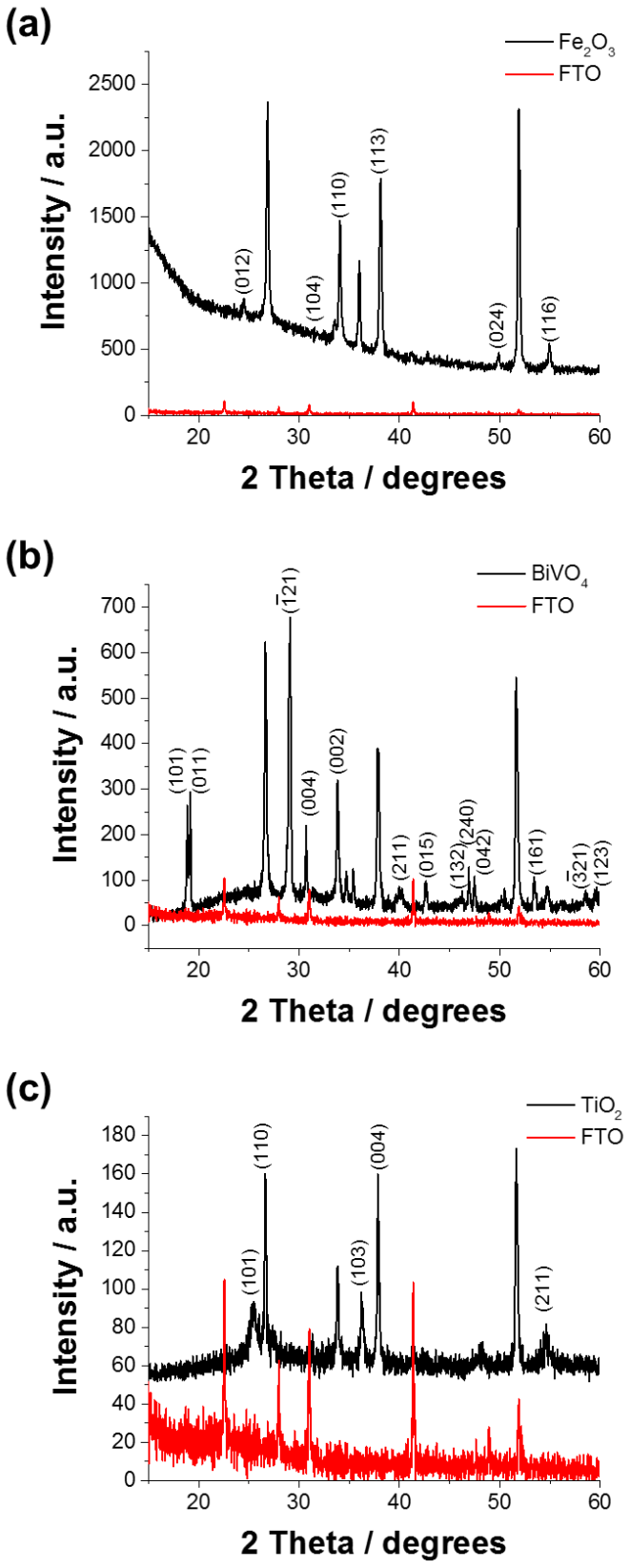

Figure 8. X-ray diffraction patterns showing the formation of various photoanodes on FTO substrate such as (a) α-Fe_2O_3 (hematite), (b) $BiVO_4$, and (c) anatase TiO_2.

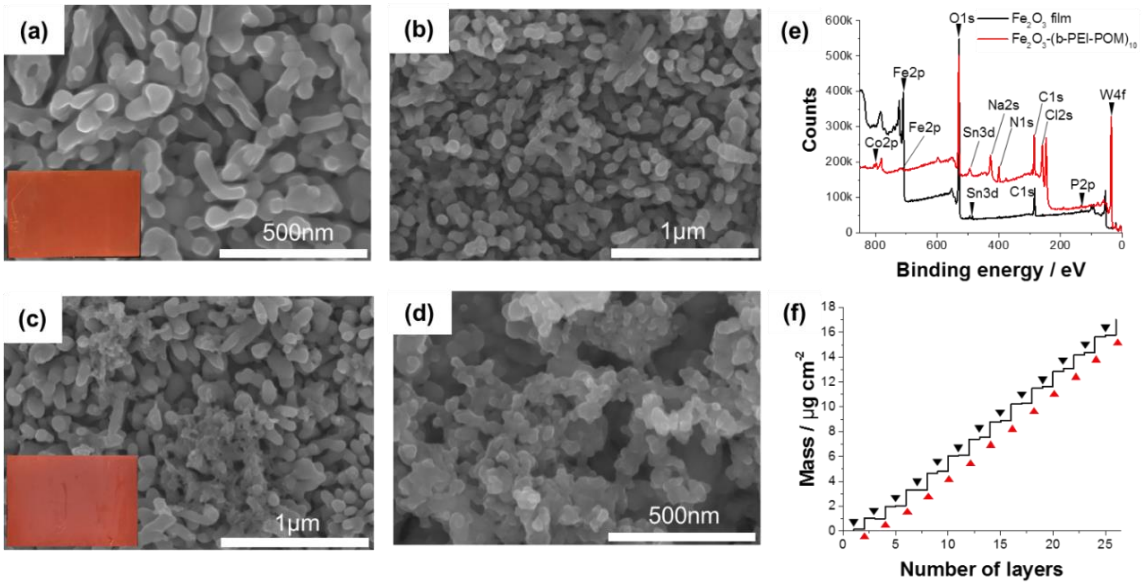

Figure 9. Formation and growth of (b-PEI/POM) layers on the hematite using the layer-by-layer assembly method. Morphology of hematite photoanodes (a) without and with (b) five, (c) ten, and (d) twenty layers of (b-PEI/POM) was imaged by scanning electron microscopy. Inset shows the corresponding photograph of the hematite electrode on the FTO substrate. (e) Elemental analysis by X-ray photoemission spectroscopy (XPS) clearly shows the increase of carbon (C), nitrogen (N), cobalt (Co), phosphorus (P), and tungsten (W) content after the deposition of $(b\text{-PEI/POM})_{10}$ layers on the hematite. (f) The formation and growth of (b-PEI/POM) layers was also studied in situ by quartz crystal microbalance (QCM). Black and red triangles indicate the introduction of polyelectrolyte and POM catalyst solutions, respectively.

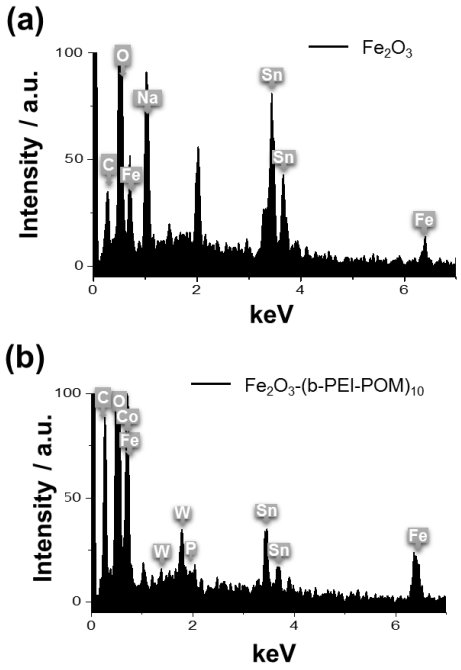

Figure 10. The formation of $(b\text{-PEI/POM})_{10}$ layers on $\alpha\text{-Fe}_2O_3$ photoanodes was also confirmed by comparing energy dispersive X-ray spectra (a) before and (b) after the LbL treatment as well as electron micrographs (Figure 9 in the manuscript).

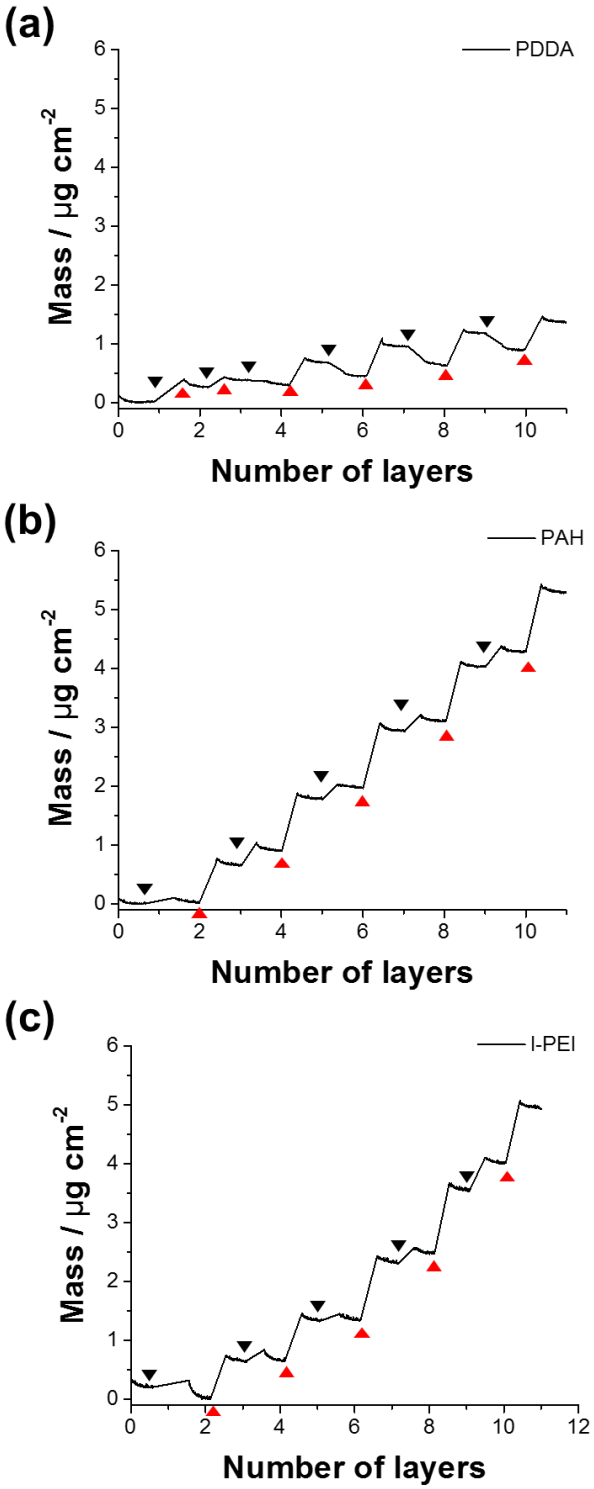

Figure 11. In situ analysis of the deposition of polyelectrolytes and POM catalysts by quartz crystal microbalance (QCM). The resonance frequency of a quartz crystal disk coated with gold electrodes was monitored in situ upon sequential treatment with solutions containing cationic polyelectrolytes (such as (a) PDDA, (b) PAH, and (c) l-PEI) and anionic POM catalysts. Black and red triangles indicate the introduction of polyelectrolyte and POM catalyst solutions, respectively.

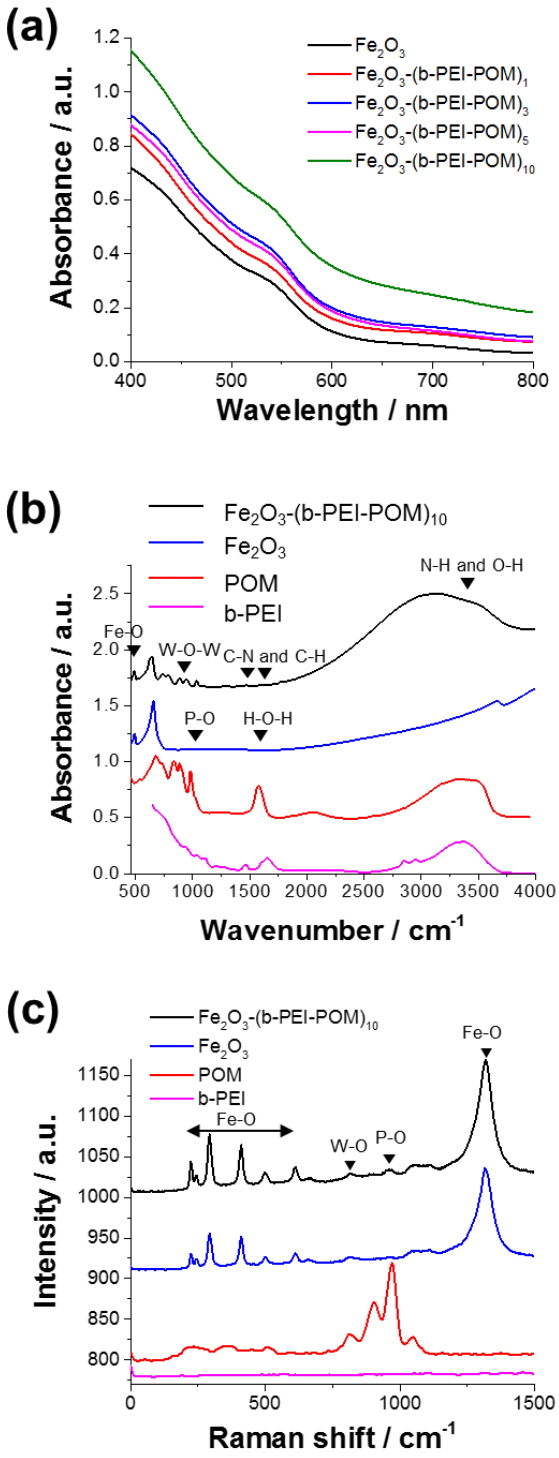

Figure 12. Formation and growth of (b-PEI/POM) layers on electrode surface using the layer-by-layer assembly method was studied ex situ by (a) UV-visible, (b) Fourier-transform infrared (FT-IR), and (c) Raman spectroscopy.

3.3 Effect of Type of Polyelectrolyte on the Performance of LbL-Modified Hematite Photoanodes

We also investigated the influence of type of cationic PE on the photoelectrochemical performance of hematite photoanode modified with (PE-POM) layers. For comparison, the concentration of each polyelectrolyte for the LbL deposition was kept constant at 3 mM in terms of monomer concentration, and the number of (PE-POM) bilayers was fixed at ten for each sample. The photoelectrochemical performance of hematite photoanodes before and after the LbL deposition was evaluated by measuring LSV (Figure 13a) and photocurrent density under an applied bias (Figure 13b) in the presence and absence of visible-light irradiation. Since we used electrically and electrochemically inactive polyelectrolytes for the integration of POM WOCs on hematite films, photoelectrochemical performances can be expected to be still unchanged or even decreased after the LbL modification. However, it was found that the performance of the hematite photoanode with (PE-POM) layers was generally improved compared to bare hematite in terms of both onset potential for water oxidation and photocurrent density, regardless of types of PEs employed (Figure 13c). Among the four different cationic PEs we tested, b-PEI was found to be most effective in terms of not only the amount of deposited POM (Figure 13d) but also the performance of photoanode after the modification (Figure 13c). Note that our result is consistent with the previous report by Toma et al. (Toma et al., 2010), which showed that cationic polyamidoamine dendrimers (structurally similar to b-PEI) can efficiently capture polyanionic POMs on the surface of multi-walled carbon nanotubes. Compared to bare Fe_2O_3, Fe_2O_3-$(b\text{-PEI/POM})_{10}$ exhibited the largest decrease of the onset potential by about 0.4 V and a significant enhancement of photocurrent density about three times with applied bias of 0.67 V vs. Ag/AgCl (1.3 V vs. RHE) at pH 8.0 under visible-light irradiation. The performance improvement by the deposition of $(PE\text{-POM})_{10}$ layers was more pronounced at lower applied bias (Figure 14). It is noteworthy here that the performance of hematite photoanode is not directly proportional to the amount of POM deposited (Figure 13d). Despite the low efficiency of l-PEI for the deposition of POM WOCs (in terms of the absolute amount of POM deposited and POM-to-polymer molar ratio), it was found to be more efficient in lowering the onset potential and raising the photocurrent density than PAH and PDDA. The structural and chemical similarity between b-PEI and l-PEI, it is thought that chemical properties of PEs may be largely affected on the photoelectrochemical responses.

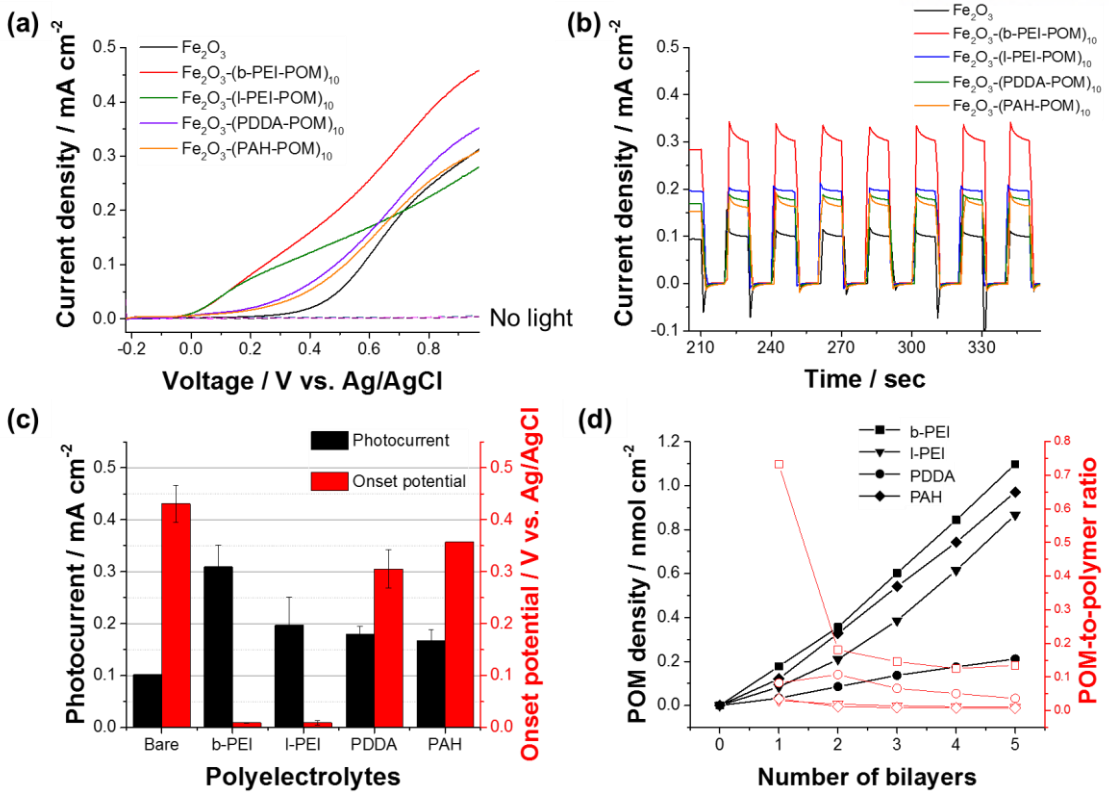

Figure 13. Influence of types of cationic polyelectrolyte on the photoelectrochemical performance of hematite photoanodes. The performance of different samples was compared by measuring (a) linear sweep voltammetry (LSV) and (b) photocurrent density under visible light illumination with an applied bias of 0.6 V vs. Ag/AgCl and (c) summarized in terms of onset potential for water oxidation and photocurrent density. (d) Graph showing the relationship between the number of bilayers (n), the areal density of POM WOCs on the hematite, and the POM-to-polymer molar ratio for different cationic polyelectrolytes.

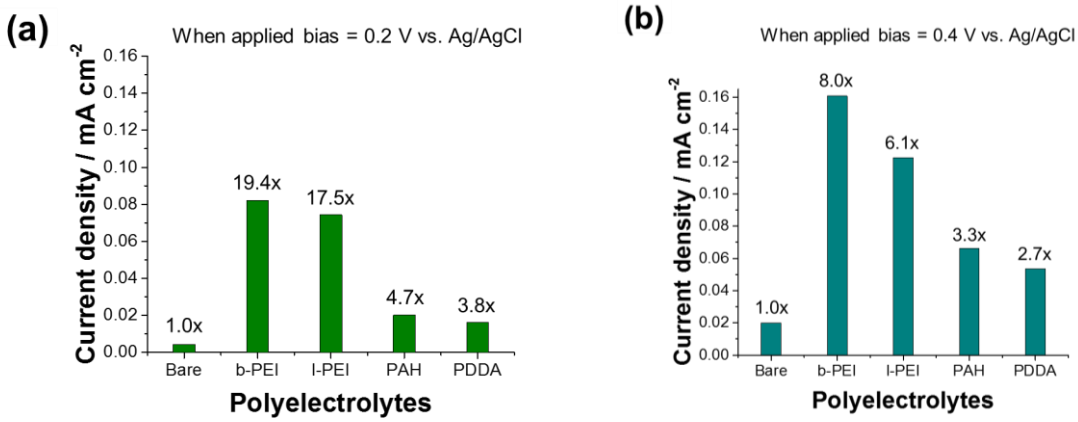

Figure 14. Influence of types of cationic polyelectrolyte on the photoelectrochemical performance (especially in terms of photocurrent density) of hematite photoanodes as a function of the applied bias. For comparison, ten bilayers of cationic polyelectrolytes and POMs were deposited on the photoanode. The numbers above each column indicate the degree of enhancement of the photocurrent density of each sample compared to that of the bare one.

3.4 Effect of the Number of the LbL Bilayers

To explain the potential role of b-PEI on the improved photocatalytic activity of hematite photoanode, we prepared four different kinds of hematite photoanodes using the LbL assembly and compared their photoelectrochemical properties (Figure 15). These include hematite photoanodes without any modification (bare Fe_2O_3), with ten layers of b-PEI and catalytically active POM (Fe_2O_3-(b-PEI/POM)$_{10}$), with ten layers of b-PEI only (Fe_2O_3-(b-PEI)$_{10}$), and with ten layers of b-PEI and polyoxometalate without tetra-cobalt active site (Fe_2O_3-(b-PEI/POM w/o Co)$_{10}$) (Figure 15a). As shown in Figure 15, the POM without the active site ($(PW_9O_{34})^{9-}$) (POM w/o Co) alone has no electrochemical catalytic activity at all. It was also found that b-PEI alone has a negligible effect on the performance of hematite photoanode. Interestingly, however, we observed that the performance of hematite photoanode was significantly improved compared to the bare counterpart below a certain potential when these two components are assembled together on the hematite surface (i.e., Fe_2O_3-(b-PEI/POM w/o CO)$_{10}$) (Figure 15b, c). This implies the synergistic effect of b-PEI and oxide clusters ($(PW_9O_{34})^{9-}$) on the performance of Fe_2O_3-(b-PEI/POM)$_{10}$. Considering that a pair of $(PW_9O_{34})^{9-}$ clusters can embed a catalytically active tetra-cobalt-oxo cluster, it is hypothesized that $(PW_9O_{34})^{9-}$ clusters can act as an efficient charge transfer bridge between hematite photoanode and the tetra-cobalt active site in the presence of b-PEI. Our hypothesis is supported by the recent report (Vasilopoulou et al., 2015) that ammonium salt of phosphotungstate can act as an efficient hole extraction layer for polymer solar cells. Further study on the observed synergistic effect by b-PEI and oxide clusters on the performance of hematite photoanode is necessary and currently under way.

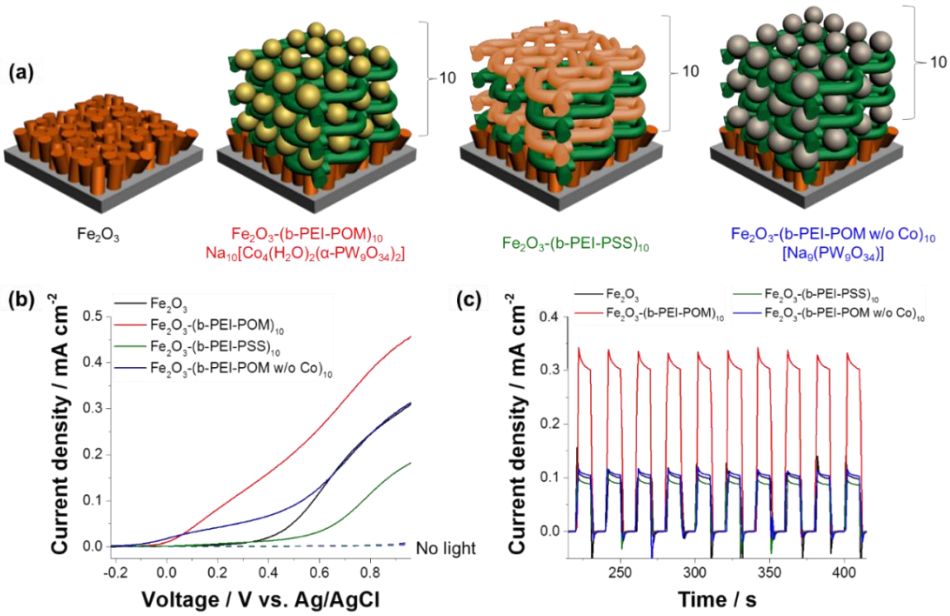

Figure 15. Effect of b-PEI on the photocatalytic activity of the hematite photoanode. To investigate the potential role of b-PEI, four different samples were prepared as shown in (a), and their photoelectrochemical performance was evaluated by measuring (b) LSV and (c) photocurrent densities in the presence and absence of visible light irradiation.

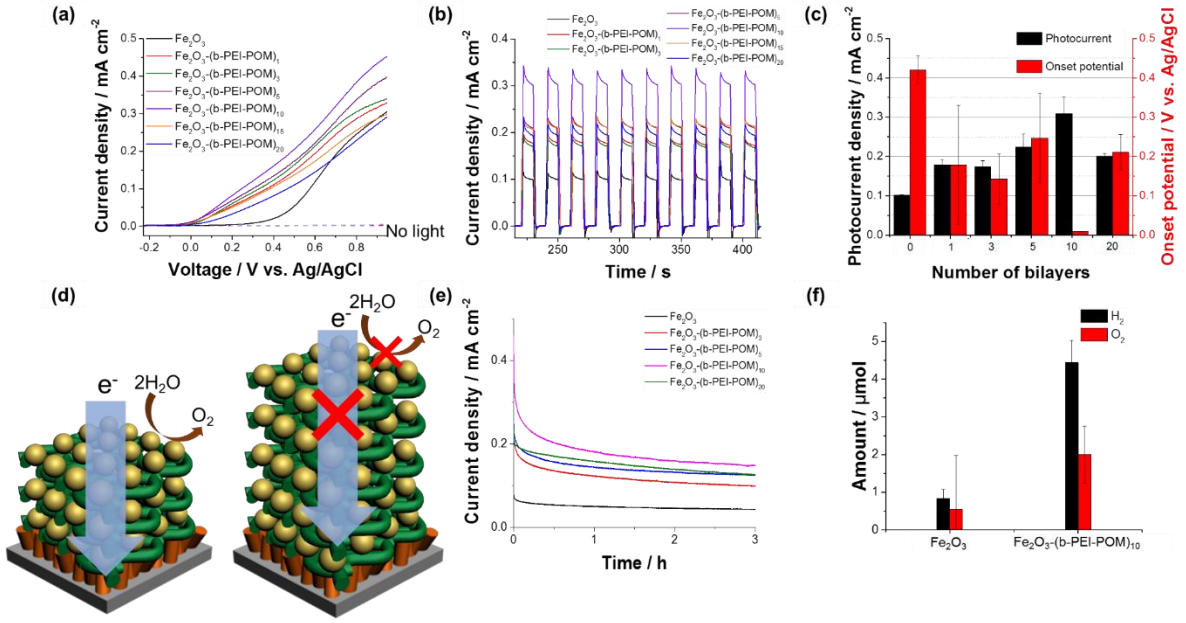

Figure 16. Effect of the number of (b-PEI/POM) layers on the photocatalytic performance of the hematite photoanode. The performance of different samples was compared by measuring (a) linear sweep voltammetry (LSV) and (b) photocurrent density under visible light illumination with an applied bias of 0.6 V vs. Ag/AgCl and (c) summarized in terms of onset potential for water oxidation and photocurrent density. (d) Mechanistic scheme explaining the degradation of photoanode performance beyond ten layers of (b-PEI/POM). A three-electrode photoelectrochemical cell was prepared to quantify the total charge transfer by (e) chronoamperogram and (f) the actual amount of gas evolved by gas chromatography to calculate the Faradaic efficiency of the hematite electrode with and without (b-PEI/POM) layers.

As a next step, we tried to find key factors affecting the performance of hematite photoanode such as the areal density of POM WOCs and the number of (b-PEI/POM) bilayers. The areal density of POM WOCs (Figure 13d) and the thickness of the (b-PEI/POM) film (data not shown) were found to be linearly proportional to the number of the bilayers. Interestingly, it was found that the photoelectrochemical performance of hematite photoanode is gradually improved upon the deposition of up to ten bilayers and then degraded when more layers are deposited (Figure 16a-c and Figure 17). Note that the performance of hematite photoanodes (e.g., Fe_2O_3-(b-PEI/POM)$_{20}$) looks degraded compared to that of the best one (i.e., Fe_2O_3-(b-PEI/POM)$_{10}$) upon LbL deposition but is still significantly improved compared to that of the bare one (i.e., Fe_2O_3). Thus, it is thought that there is a critical thickness of the bilayer, below which photogenerated holes on hematite can be efficiently scavenged by POM WOCs for oxidation of water (Figure 16d). To exclude the possibility that the observed improvement in photoelectrochemical performance of hematite photoanode is resulted from undesirable side reactions such as oxidation of PEs and photocorrosion of hematite, we measured the Faradaic efficiency of hematite photoanode for water oxidation before and after the LbL modification.

The chronoamperogram of hematite photoanode showed a gradual decrease of photocurrent density over time, but the overall tendency of the effect of the number of bilayers remained unchanged (Figure 16e). As expected from LSV and photocurrent measurement, the amount of oxygen and hydrogen evolved was significantly increased after the modification with (b-PEI/POM) layers (Figure 16f). The Faradaic efficiencies of hematite photoanode before and after modification with $(\text{b-PEI/POM})_{10}$ layers were found to be 55 and 94 percent, respectively, with an applied bias of 0.77 V vs. Ag/AgCl under visible light irradiation at pH 8.0. For Fe_2O_3-$(\text{b-PEI/POM})_{10}$, the turnover frequency (TOF) for oxygen evolution by POM was found to be 3.37×10^2 h^{-1} under the same condition. The detailed mechanism of charge transfer between hematite and POM remains unclear at the current stage. But, one can speculate that hematite photoanode may not be completely covered by a single-cycle of bilayer deposition and/or that '*flexible*' polymer chains not only act as an efficient electrostatic adhesive for POM WOCs, but also facilitate the charge-transfer interaction between the photoanode and POM WOCs.

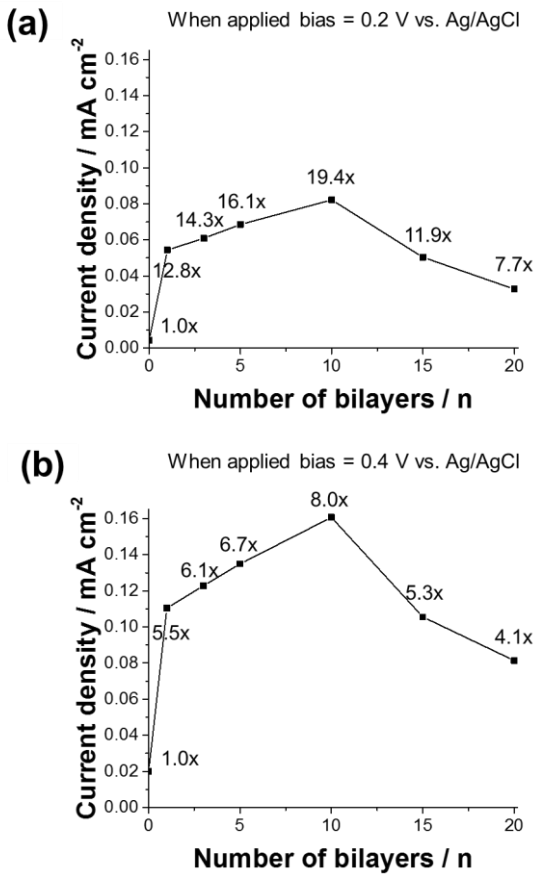

Figure 17. Effect of the number of (b-PEI/POM) bilayers (n) on the photoelectrochemical performance (especially in terms of photocurrent density) of hematite photoanodes as a function of the applied bias. The numbers above each point indicate the degree of enhancement of the photocurrent density of each sample compared to that of the bare one.

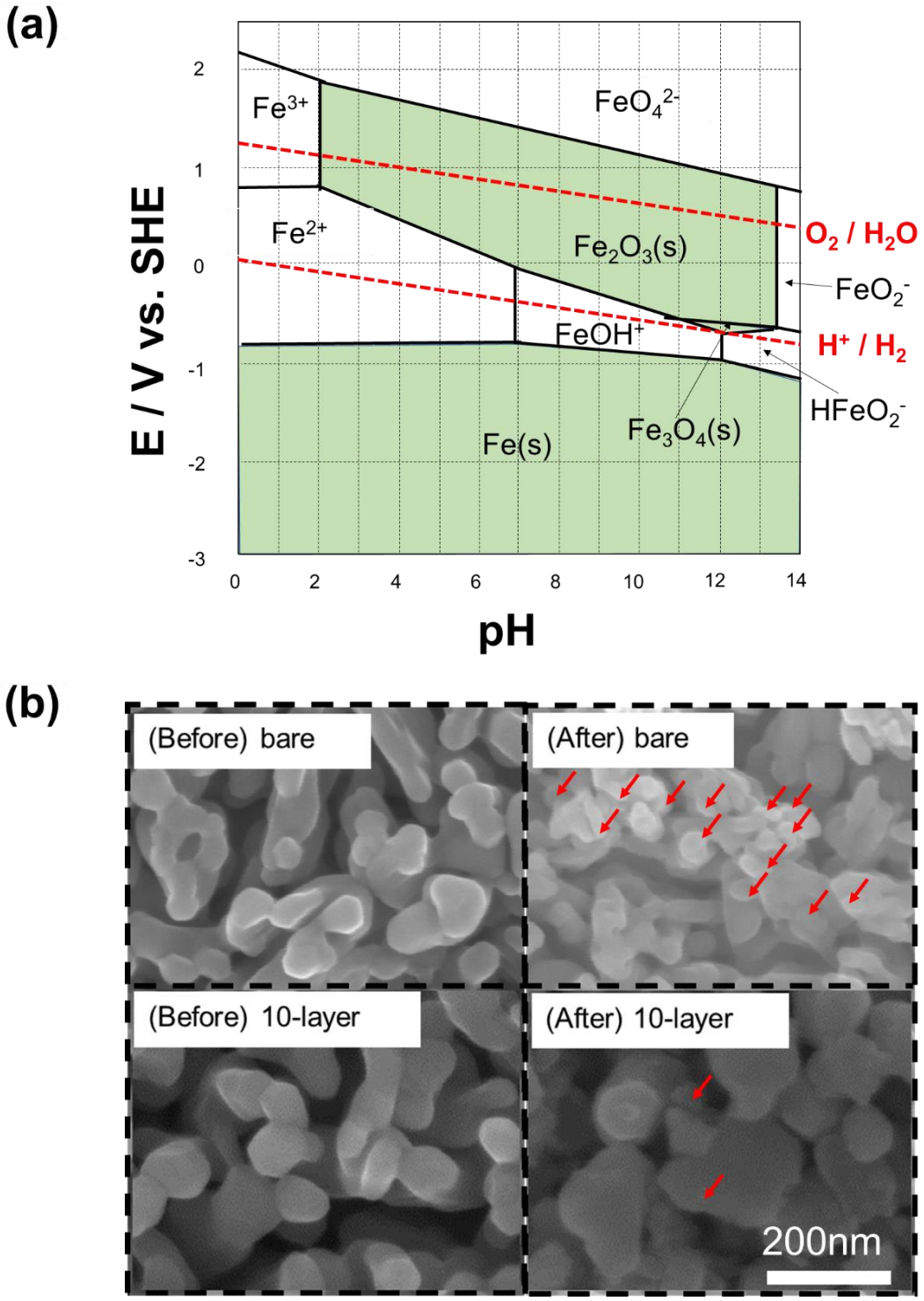

Figure 18. Stability of hematite photoanodes with and without $(b\text{-PEI/POM})_{10}$ layers. (a) The Pourbaix diagram for Fe-H_2O was obtained from the Materials Project database (http://www.materialsproject.org). (b) SEM micrographs of hematite with and without $(b\text{-PEI/POM})_{10}$ layers were compared before and after the photoelectrochemical test for 1 h with an applied bias of 0.6 V vs. Ag/AgCl under visible light irradiation to study the effect of $(b\text{-PEI/POM})_{10}$ layers on the stability of hematite photoanodes.

Since the low Faradaic efficiency of bare hematite implies the presence of unwanted side reactions such as photocorrosion of photoanodes (Chen et al., 2013), we studied the morphology of hematite photoanode before and after the photocatalytic water oxidation for three hours in the presence and absence of $(b\text{-PEI/POM})_{10}$ layers. According to the literature (Kim et al., 2014) and the Pourbaix diagram (Walter et al., 2010; Park et al., 1979; Li et al., 2013) (Figure 18a), hematite exhibits a poor stability at around neutral pHs due to cathodic corrosion. The bare hematite (Fe_2O_3) showed a clear morphological change after the reaction such as fragmentation of hematite crystals possibly due to its photocorrosion (Figure 18b). On contrary, Fe_2O_3-$(b\text{-PEI/POM})_{10}$ exhibited a negligible morphological change after the reaction as expected from its high Faradaic efficiency (Figure 18b). Considering the cathodic corrosion of hematite at near-neutral pHs and hole-scavenging activity of POMs, the observed stability improvement of hematite photoanode is attributed to the formation of (b-PEI/POM) layers, especially b-PEI layers. It is interesting to point out that according to our results, b-PEI plays multiple vital roles in the improvement of the overall performance of hematite photoanodes: (1) an electrostatic adhesive for POM WOCs, (2) an agent for improving charge transfer between hematite photoanode and POM WOCs, and (3) a protective coating layer against the corrosion of hematite photoanode.

3.5 LbL-Modification of Various Photoanode Materials

Lastly, to demonstrate the versatility of our approach for the substrate-independent assembly of various functional components for the construction of a photosynthetic device, we prepared various forms of photoanodes by the LbL modification of various photoanodes such as Fe_2O_3, $BiVO_4$ and TiO_2. We first tried to deposit a different polyoxometalate WOC, $[Co_4(H_2O)_2(VW_9O_{34})_2]^{10-}$ (POM(V)) (Lv H. et al., 2014), which is structurally very similar to the POM we have used, $[Co_4(H_2O)_2(PW_9O_{34})_2]^{10-}$. It was found that although POM(V) had a much higher catalytic activity than POM as shown in Figure 7, POM(V) was found to be less active when integrated on the surface of hematite photoanode using LbL assembly method (Figure 19). This result indicates that the integration of WOCs with a higher catalytic activity does not guarantee a higher overall performance of a photosynthetic device and that it is important to build and test an actual device in various combinations to find a better photosynthetic device. As a next step, we tried to integrate POM WOCs on different photoanode materials such as $BiVO_4$ (Li et al., 2014; Kim and Choi, 2014) and TiO_2 (Chen et al., 2010), which are also well-known as a promising photoanode material for solar water oxidation, and carefully examined their photocatalytic properties. They were synthesized according to the literature (Kim and Choi, 2014; Hoang et al., 2013), and their formation was confirmed by XRD (Figure 20). We could readily deposit multiple bilayers of b-PEI and POM WOCs on $BiVO_4$ (Figure 21a-c and Figure 20a-b) and TiO_2 (Figure 21d-f and Figure 20c-d), respectively, and successfully improve their photocatalytic properties in terms of onset potential and photocurrent density in a way similar to that of hematite (Table 2). Encouraged by such results, we are currently attempting to integrate various functional components such as carbon

nanomaterials and metal nanoparticles to make a more efficient photosynthetic device. It was found that our approach also works well for these cases (data not shown). A more detailed study about this is currently under way and will be reported in the future. Although here we only demonstrated the validity of our LbL-based approach for the construction of an oxidation half-reaction device with a few components, in principle, it can be also utilized to design and build various novel electrochemical and photoelectrochemical devices. That is because it allows us to precisely assemble multiple components in various combinations without altering their properties in a desired order on any kinds of substrates (Xiao et al., 2016). In this regard, we believe that our approach not only provide an alternative way to build a photosynthetic device but also enables design and realization of novel electrochemical and photoelectrochemical devices by taking advantage of the huge library of each component.

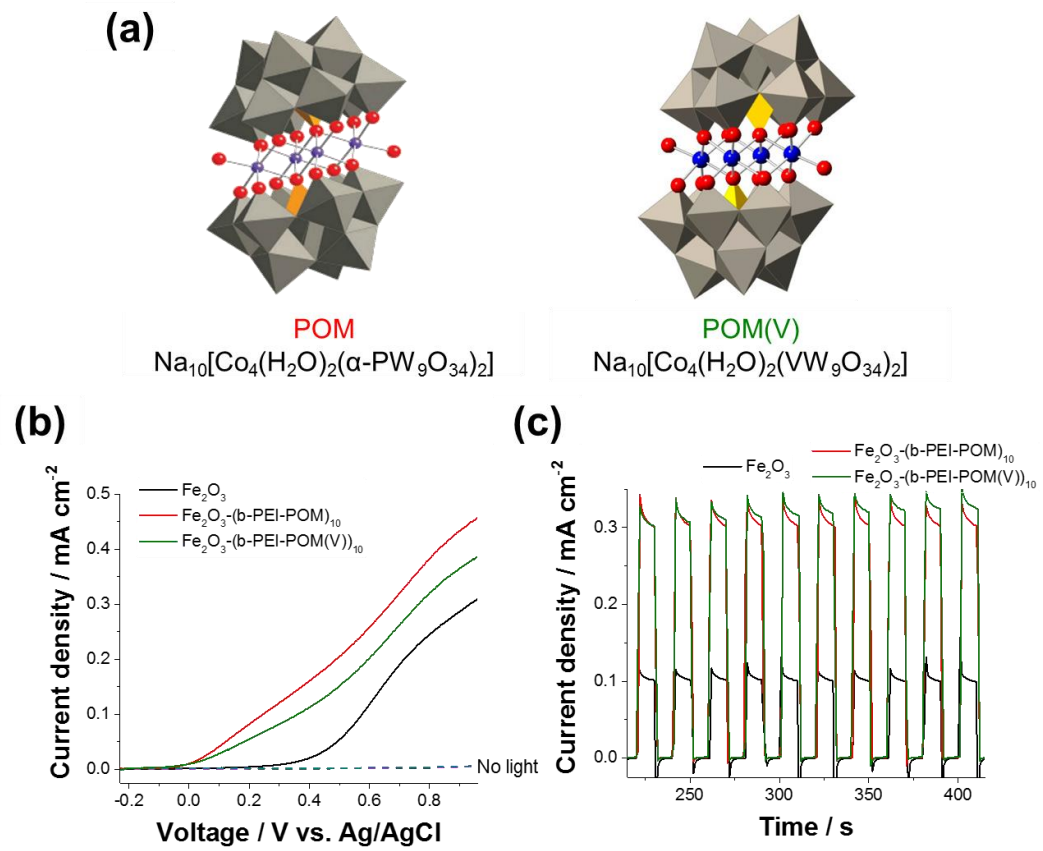

Figure 19. Photoelectrochemical performance of hematite photoanodes after the deposition of different polyoxometalate catalysts. Although POM(V) had a much higher catalytic activity than POM(P), as shown in Figure 7, POM(V) was found to be less active when integrated on the surface of the hematite photoanode using the LbL assembly method. (a) Molecular structure of POM(P) and POM(V). The photocatalytic performance of each sample was analyzed by measuring (b) linear sweep voltammetry and (c) photocurrent density.

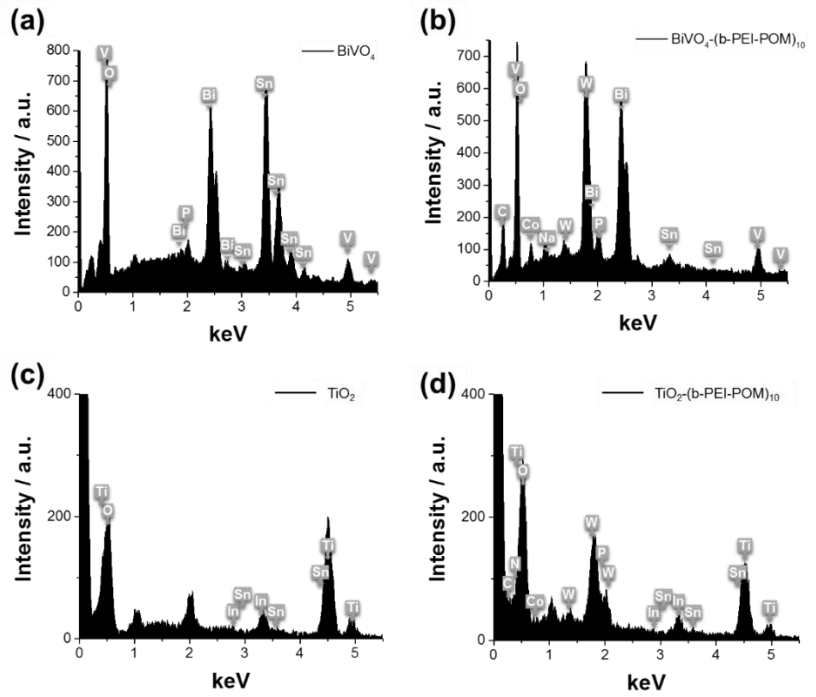

Figure 20. The formation of $(b\text{-PEI/POM})_n$ layers on (a, b) $BiVO_4$ and (c, d) TiO_2 photoanodes was confirmed by comparing energy dispersive X-ray spectra (a, c) before and (b, d) after the LbL treatment, as well as electron micrographs (Figure 20 in the manuscript). Note that the numbers of (b-PEI/POM) bilayers (n) formed on $BiVO_4$ and TiO_2 photoanodes are 10 and 5, respectively.

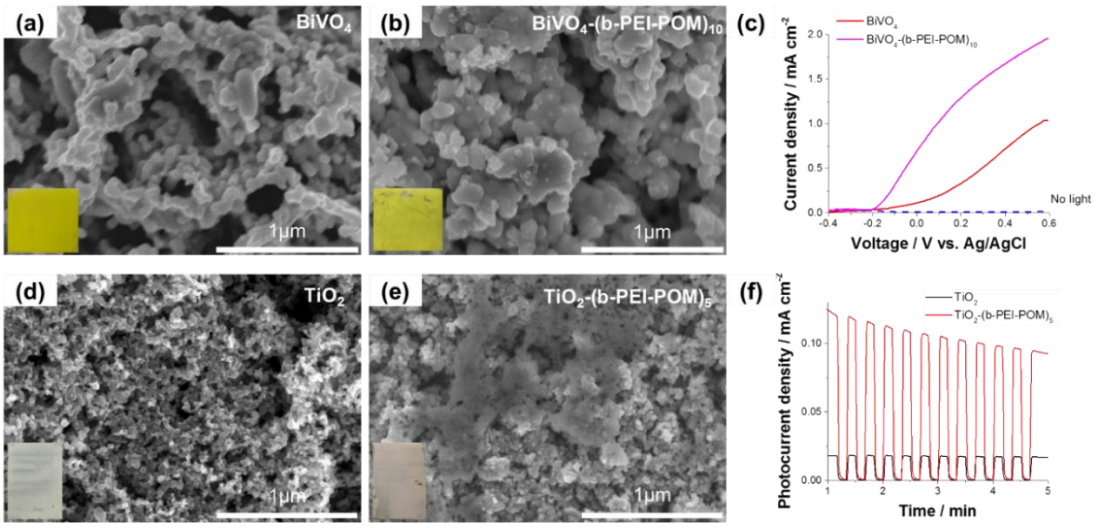

Figure 21. Improvement of the performance of (a-c) $BiVO_4$ and (d-f) TiO_2 photoanodes by layer-by-layer (LbL) assembly of cationic polyelectrolyte b-PEI and anionic POM water oxidation catalysts (WOCs). The formation of $(b\text{-PEI/POM})_n$ layers on $BiVO_4$ (n=10) and TiO_2 (n=5) photoanodes was confirmed by (a, b, d, e) electron microscopy, respectively, (a, d) before and (b, e) after the LbL treatment. (c, f) The effect of the $(b\text{-PEI/POM})_n$ layers on the performance of (c) $BiVO_4$ and (f) TiO_2 photoanodes was studied by measuring the linear sweep voltammetry (LSV) and photocurrent density with and without light irradiation. Note that visible and UV light was illuminated for $BiVO_4$ and TiO_2, respectively.

Table 2. Enhancement of photoelectrochemical performance of $BiVO_4$ and TiO_2 photoanodes by the deposition of (b-PEI/POM) layers.

	Bare		**After modification with $(b\text{-PEI/POM})_n$**		**Enhancement**	
	Onset potential / V vs. Ag/AgCl	Photocurrent density / mA cm^{-2}	Onset potential / V vs. Ag/AgCl	Photocurrent density / mA cm^{-2}	Onset potential shift / V	Photocurrent density / %
$BiVO_4$ (n = 10)	0.0043	1.036	-0.192	1.9558	0.1963	189
TiO_2 (n = 5)	-0.78	0.0177	-0.9	0.105	0.12	593

IV. CONCLUSION

In conclusions, we successfully fabricated more efficient photoanodes for producing electrons and protons with high efficiency which lead to efficient hydrogen evolution reaction using simple and versatile, LbL method. Various cationic polyelectrolytes, branched PEI, linear PEI, PDDA and PAH and anionic POMs, POM, POM(V) and POM w/o Co could be efficiently integrated on various types of substrates such as Fe_2O_3, Au, $BiVO_4$ and TiO_2 under light illumination. It was found that their photoelectrochemical properties could be engineered by controlling various factors of LbL assembly such as types of PEs, areal density of catalysts deposited on substrates, and the number of deposited layers of LbL films. Regardless of types of substrates, after LbL modification with WOCs, photoelectrochemical responses such as LSV or photocurrent areal density were significantly enhanced compared to bare films. It seems to overcome the weakness which is relatively lower photoelectrochemical performances by applying LbL method. Considering the versatile nature of LbL assembly for the deposition of multiple functional materials with diverse size and shape in various combinations, it is thought that our LbL-based approach can not only provide a general and simple method for the controlled assembly of them to make an artificial photosynthetic device, but also enable designing of a novel electrochemical/photoelectrochemical system.

V. REFERENCES

1. Chen, C., et al. **(2014)**. "A prodrug strategy based on chitosan for efficient intracellular anticancer drug delivery." *Nanotechnology* 25(25): 255101.
2. Chen, X., et al. **(2010)**. "Semiconductor-based photocatalytic hydrogen generation." *Chemical Reviews* 110(11): 6503-6570.
3. Chen, Z., et al. **(2013)**. *Photoelectrochemical water splitting : standards, experimental methods, and protocols*. Springer: New York, 2013; p x: 126 p.
4. Ciamician, G. **(1912)**. "The Photochemistry of the Future." *Science* 36(926): 385-394.
5. Clifford, J. N., et al. **(2009)**. "Electron transfer dynamics in dye-sensitized solar cells utilizing oligothienylvinylene derivates as organic sensitizers." *ChemSusChem* 2(4): 344-349.
6. Cox, N., et al. **(2015)**. "Artificial photosynthesis: understanding water splitting in nature." *Interface Focus* 5(3): 20150009.
7. Hammarston, L.; Hammes-Schiffer, S. **(2009)**. "Artificial photosynthesis and solar fuels." *Accounts of Chemical Research* 42: 1859.
8. Hammarstrom, L., et al. **(2011)**. "Shedding light on solar fuel efficiencies." *Science* 333(6040): 288.
9. Hoang, T. T., et al. **(2013)**. "Enhanced Charge Transfer of Liquid and Gel Electrolytes Using Nano Platinum in Dye-sensitized Solar Cells." *Ieee Phot Spec Conf*: 2713-2715.
10. Holladay, J.D., et al. **(2009)**. "An overview of hydrogen production technologies." *Catalysis Today* 139: 244-260.
11. Ilbas, M., et al. **(2005)**. "Investigations of hydrogen and hydrogen-hydrocarbon composite fuel combustion and NOx emission characteristics in a model combustor." *International Journal of Hydrogen Energy* 30: 1139-47.
12. Jang, J. W., et al. **(2015)**. "Enabling unassisted solar water splitting by iron oxide and silicon." *Nature Communications* 6: 7447.
13. Johannsmann, D., *The quartz crystal microbalance in soft matter research*. Springer Berlin Heidelberg: New York, NY, 2014; p pages cm.
14. Jubb, A.M., et al. **(2010)**. "Vibrational spectroscopic characterization of hematite, maghemite, and magnetite thin films produced by vapor deposition." *Applied Materials and Interfaces* 2(10): 2804-2812.
15. Katz, M. J., et al. **(2015)**. "Dynamics of Back Electron Transfer in Dye-Sensitized Solar Cells Featuring 4-tert-Butyl-Pyridine and Atomic-Layer-Deposited Alumina as Surface Modifiers." *Journal of Physical Chemistry B* 119(24): 7162-7169.
16. Kim, D., et al. **(2015)**. "Artificial photosynthesis for sustainable fuel and chemical production."

Angewandte Chemie International Edition 54(11): 3259-3266.

17. Kim, J. Y., et al. **(2013)**. "Single-crystalline, wormlike hematite photoanodes for efficient solar water splitting." *Scientific Reports* 3: 2681.
18. Kim, J. Y., et al. **(2014)**. "A Stable and Efficient Hematite Photoanode in a Neutral Electrolyte for Solar Water Splitting: Towards Stability Engineering." *Advanced Energy Materials* 4(13), 1400476.
19. Kim, T. W. and K. S. Choi **(2014)**. "Nanoporous $BiVO_4$ photoanodes with dual-layer oxygen evolution catalysts for solar water splitting." *Science* 343(6174): 990-994.
20. Lauinger, S. M., et al. **(2015)**. "High Stability of Immobilized Polyoxometalates on TiO_2Nanoparticles and Nanoporous Films for Robust, Light-Induced Water Oxidation." *Chemistry of Materials* 27(17): 5886-5891.
21. Li, Z., et al. **(2013)**. "Photoelectrochemical cells for solar hydrogen production: current state of promising photoelectrodes, methods to improve their properties, and outlook." *Energy Environmental Sciences* 6(2): 347-370.
22. Liu, R., et al. **(2012)**. "Facile synthesis of Au-nanoparticle/polyoxometalate/graphene tricomponent nanohybrids: an enzyme-free electrochemical biosensor for hydrogen peroxide." *Small* 8(9): 1398-1406.
23. Lv, H., et al. **(2014)**. "An exceptionally fast homogeneous carbon-free cobalt-based water oxidation catalyst." *Journal of the American Chemical Society* 136(26): 9268-71.
24. Macon, A. L., et al. **(2016)**. "Reversible assembly of pH responsive branched copolymer-stabilised emulsion via electrostatic forces." *Chemical Communications* 52(1): 136-139.
25. Ming, Q., et al. **(2002)**. "Steam reforming of hydrocarbon fuels." *Catalysis Today* 77: 51-64.
26. Molchan, I.S., et al. **(2013)**. "Corrosion behavior of mild steel in 1-alkyl-3-methylimidazolium tricyanomethanide ionic liquids for CO_2 capture applications." *RSC Advances* 4: 5300-5311.
27. Orlandi, M., et al. **(2010)**. "Ruthenium polyoxometalate water splitting catalyst: very fast hole scavenging from photogenerated oxidants." *Chemical Communications* 46(18): 3152-4.
28. Ozzie, Z. **(2012)** *Green Illusions*, Lincoln and London: University of Nebraska Press. pp. 1-169, 331-42.
29. Park, S. M., et al. **(1979)**. "Thermodynamic Stabilities of Semiconductor Electrodes." *Journal of Electroanalytocal Chemistry* 99(1): 67-75.
30. Roger, I., et al. **(2017)**. "Earth-abundant catalysts for electrochemical and photoelectrochemical water splitting." *NATURE REVIEWS* 1(00003).
31. Ryu, J., et al. **(2014)**. "Biocatalytic photosynthesis with water as an electron donor." *Chemistry – A European Journal* 20(38): 12020-12025.
32. Sartorel, A., et al **(2008)** "Polyoxometalate embedding of a tetraruthenium(IV)-oxo-core by template-directed metalation of [gamma-SIW10O36](8-): A totally inorganic oxygen-evolving catalyst." *Journal of the American Chemical Society* 130(15), 5006-????.

33. Shen, S. et al., **(2013)**. “Facile growth a porous hematite films for photoelectrochemical water splitting.” *International Journal of Photoenergy* :174981.
34. Sivula, K. et al., (2011). “Solar water splitting: progress using hematite (alpha-Fe(2) O(3)) photoelectrodes.” *ChemSusChem* 4 (4): 432-49.
35. Shimada, T., et al. **(2012)**. "How is the water molecule activated on metalloporphyrins? Oxygenation of substrates induced through one-photon/two-electron conversion in artificial photosynthesis by visible light." *Faraday Discuss* 155: 145-163; discussion 207-122.
36. Suarez-Guevara, J., et al. **(2014)**. "Stable graphene-polyoxometalate nanomaterials for application in hybrid supercapacitors." *Phys Chem Chem Phys* 16(38): 20411-20414.
37. Tachibana Y., et al. **(2012)** Artificial photosynthesis for solar water-splitting, *Nature Photonics* 6: 511.
38. Tamirat A.G., et al. **(2016)**. “Using hematite for photoelectrochemical water splitting: a review of current progress and challenges.” *Nanocscale Horizon* 1: 243-267.
39. Tilley, S. D., et al. **(2010)**. “Light-induced water splitting with hematite: improved nanostructure and iridium oxide catalysis.” *Angewandte Chemie International Edition* 49(36): 6405-8.
40. Toma, F. M., et al. **(2010)**. "Efficient water oxidation at carbon nanotube-polyoxometalate electrocatalytic interfaces." *Nature Chemistry* 2(10): 826-31.
41. Wang, C., et al. **(2011)**. "Doping metal-organic frameworks for water oxidation, carbon dioxide reduction, and organic photocatalysis." *Journal of the American Chemical Society* 133(34): 13445-13454.
42. Vasilopoulou, M., et al., **(2015)**. “Annealing-free highly crystalline solution-processed molecular metal oxides for efficient single-junction and tandem polymer solar cells.” *Energy Environ Sci* 8(8): 2448-63.
43. Walter, M. G., et al. **(2010)**. "Solar Water Splitting Cells." *Chemical Reviews* 110(11): 6446-6473.
44. White, J. L., et al. **(2015)**. "Light-Driven Heterogeneous Reduction of Carbon Dioxide: Photocatalysts and Photoelectrodes." *Chemical Reviews* 115(23): 12888-12935.
45. Xiao, F. X., et al. **(2016)**. "Layer-by-layer assembly of versatile nanoarchitectures with diverse dimensionality: a new perspective for rational construction of multilayer assemblies." *Chemical Society Reviews* 45(11): 3088-121.
46. Yin, Q. S., et al. **(2010)**. "A Fast Soluble Carbon-Free Molecular Water Oxidation Catalyst Based on Abundant Metals." *Science* 328(5976): 342-345.

ACKNOWLEDGEMENTS

대학을 졸업하고도 벌써 2 년이라는 세월이 흘렀습니다. 부족한 점도 많고 배워야 할 것도 많았던 저에게 인내와 믿음으로 가르침을 주신 지도교수님, 류정기 교수님께 먼저 진심으로 감사인사 올립니다. 내일부터가 아니라 오늘부터 열심히, 더 잘 하는 성실한 학생이 되도록 하겠습니다.

구술발표 때 아낌없는 조언을 주셨던 송현곤 교수님과 김병수 교수님, 정말 감사했습니다. 주셨던 조언을 토대로 앞으로 더 발전하는 학생이 되도록 노력하겠습니다.

그리고, 실험 많이 도와줬던 연구실 학생들과 연구실에서 힘이 돼 주었던 대학원 전우들, 앞으로도 서로에게 자극이 되고 도움이 되길 바랍니다.

엄마 아빠 저 졸업합니다. 이만큼 키우느라 고생하셨고, 항상 존경하고 말로 다 할 수 없을 만큼 사랑해요.